Scientific Reports

https://doi.org/10.1038/s41598-026-62629-6

Article in Press

# Adsorption behavior of lead and chromium onto MgO impregnated biochar derived from banana peels and rice husk in binary environment

Received: 16 March 2026

Accepted: 13 July 2026

Published online: 16 July 2026

Cite this article as: Kanwal T., Iftikhar R., Ernst M. *et al.* Adsorption behavior of lead and chromium onto MgO impregnated biochar derived from banana peels and rice husk in binary environment. *Sci Rep* (2026). https://doi.org/10.1038/s41598-026-62629-6

**Tayyaba Kanwal, Rashid Iftikhar, Mathias Ernst, Kang Hoon Lee & Muhammad Ali Inam**

# Adsorption behavior of lead and chromium onto MgO impregnated biochar derived from banana peels and rice husk in binary environment

Tayyaba Kanwal[a], Rashid Iftikhar[a], Mathias Ernst[b]; Kang Hoon Lee[c*] and Muhammad Ali Inam[a,b*]

[a] *School of Civil and Environmental Engineering (SCEE), Institute of Environmental Sciences and Engineering (IESE), National University of Sciences and Technology (NUST), Islamabad 44000, Pakistan.*

[b] *Institute for Water Resources and Water Supply, Hamburg University of Technology, Am Schwarzenberg-Campus 3, 21073, Hamburg, Germany*

*c Department of Energy and Environmental Engineering, The Catholic University of Korea, Seoul 14662, Republic of Korea*

**Corresponding authors: Muhammad Ali Inam (ainam@iese.nust.edu.pk, muhammad.ali.inam@tuhh.de); Kang Hoon Lee (diasyong@catholic.ac.kr); Tel.: +49 (0)40 30601-3919; +82-2-2164-4859*



## Abstract

In current research, raw- and MgO- impregnated biochar derived via (co)pyrolysis of rice husk (RH) and banana peel (BP) in mass ratios (0:1, 1:0 and 1:1) were synthesized and examined for their physiochemical properties and adsorption performance for Cr(VI) and Pb(II) ions removal from synthetic solutions. Owing to excellent removal capability (Cr(VI): 94% at pH 2; Pb(II): 100% at pH 4) of 2 g/L MgO- impregnated biochar with mass ratio 1:1 (MgO@CBC) for 20 mg/L metals ions loading in single solute system with 120 min contact time, removal performance of

MgO@CBC was examined under binary environment. Interestingly, binary solute system showed significant MgO@CBC adsorption performance for Pb(II) removal (99%) with slight decrease in Cr(VI) removal (88.5%) at pH 2 under similar boundary conditions. Moreover, increasing metal ions concentration showed improved MgO@CBC adsorption potential for Cr(VI) at pH 4 and Pb(II) at pH 2, due to porous matrix $Mg^{2+}$-mediated compounds and unique surface characteristics. Furthermore, the underlying removal mechanism using MgO@CBC was identified as (Cr(VI): reduction/complexation coupled with electrostatic attraction) and (Pb(II): ligand exchange followed by surface complexation) and in binary system as (Cr(VI) and Pb(II): ligand exchange, electrostatic attraction, bimetallic bonding (Pb-O-Cr) and surface complexation). In addition, MgO@CBC displayed promising recyclability potential for metal ions removal up to five cycles. In general, these experimental and mechanistic insights may provide feasible and ecofriendly solutions to tanneries, when dealing with toxic metal ions from their effluents.

*Keywords:* Agri-based biochar, Co-pyrolysis, Cr(VI)/Pb(II) adsorption, MgO activation, Removal mechanism, Wastewater treatment.



## 1. Introduction

Wastewater reclamation and treatment are crucial to ensure a sustainable water source for human and agricultural practices [1]. Among various wastewater effluents, tannery industry is responsible for degradation of water reservoirs and surrounding environment, specifically in the economic zones of Pakistan. Over 600 tanneries in Kasur, Karachi and Sialkot are mainly responsible for discharging their untreated wastewater into open fields, waterways and unauthorized disposal sites [2]. Among various pollutants in tannery effluents, heavy metals have been found to be much higher up to 1000 times higher in order of magnitude than that of safe limit. For instance, water bodies surrounding industrial regions of Pakistan indicate high level

contamination with 1.99 mg/L to 13.53 mg/L Cr(VI) and 0.03 mg/L to 0.74 mg/L Pb(II) concentrations, respectively [3], [4]. In addition, soil contamination levels also indicate Cr(VI) levels from 6,900 to 19,500 mg/kg and Pb(II) contamination from 1 to 15 mg/kg [3], [4]. Exposure to such higher levels of both Pb(II) and Cr(VI) poses serious threats to human health, which might include lung cancer, irritation and inflammation of skin, respiratory problems and physiological damage [5], [6]. In accordance, due to their detrimental effects, the World Health Organization (WHO), United States Environmental Protection Agency (USEPA) and Pakistan National Environmental Quality Standards (Pak-NEQS) have been strictly restricted to the limits in wastewater for Cr(VI) as 0.05 mg/L, 0.1 mg/L and 1 mg/L, respectively and for Pb(II) as 0.01 mg/L, 0.05 mg/L and 0.5 mg/L, respectively [7]. Therefore, there is an urgent need to provide practical solutions to the tannery industry to deal with heavy metal contamination for ensuring sustainable livelihood and cleaner industrial practices.

A variety of treatment strategies including coagulation, electrochemical separation, biochemical processes and membrane technology have been previously employed to remove the intended metal ions (both Cr and Pb) from wastewater. However, these treatment techniques have various limitations including high operating costs, more sludge generation, biological toxicity, system complexities etc. [8], [9]. In contrast, adsorption is the preferred treatment technique due to its simplicity, cost effectiveness, efficiency, wide applicability, and environmentally friendly nature. Previously, a variety of adsorbent materials including algal biomass-based [10], nanomaterials-based [11], polymer-based composites[12] and agricultural byproducts[13] have been developed and examined for their efficiency in removing targeted metal ion species, i.e., Cr(VI) and Pb(II) from wastewater sources. For instance, algal biomass, exemplified by *Sargassum dentifolium (*1.5 g), exhibited 99.68% Cr(VI) removal at 100 mg/L initial Cr(VI)

concentration, pH (7) and contact time (1hour), while 1 g/L *Gelidium amansii* showed 100% Pb(II) removal at 200 mg/L initial Pb(II) concentration, pH (4.5) and 1 hour contact time [14]. However, preparation and growth procedures of algal biomasses restrict its potential for subsequent utilization as potential adsorbent in removing heavy metal ions for large scale operations. In addition, magnetite-incorporated multi-walled carbon nanotube (MWCNT) nanocomposites (1:2), synthesized via chemical vapor deposition and wet impregnation, demonstrated remarkable efficiencies of over 97% for Cd(II) and Ni(II), 100% for Pb(II), and 97.99% for Cr(VI) from petroleum-contaminated wastewater [15]. Despite such high efficiency, the complicated synthesis approach could limit its economic feasibility for large-scale applications. Moreover, concerns regarding the recovery and environmental impact of MWCNT-based nanomaterials remain. Further, the polyaniline-coated iron ore mining waste composite (PANI@IOMW) achieved up to 99% Cr(VI) removal under optimal conditions (pH 2, 0.15 g dose, 90 min) [16]. Still, its reusability was limited to two cycles, due to polyaniline degradation under acidic conditions, resulting in possible aniline leaching and reduced stability. Therefore, finding sustainable wastewater treatment options is imperative and demands affordable adsorbents with minimal pretreatment requirements. In lieu, agricultural biomass-based adsorbents may offer a groundbreaking solution, combining economic viability, environmental sustainability and technical efficiency. Consequently, leveraging its potential adsorption capability and effectiveness, a transformative wastewater treatment paradigm that addresses environmental and wastewater challenges with consideration of circular economy, needs to be established [17]. Previous research has shown applications of distinct agro-waste-derived biosorbents for wastewater treatment. For instance, Ashfaq[18] synthesized $TiO_2$ nanoparticles incorporated (potato peels: banana peels; 50:50) biomasses-based biochar and achieved 91% Pb(II) removal from synthetic test solutions. However,

various challenges including $TiO_2$ nanoparticles agglomeration behavior in treated water and unclear adsorption mechanisms hinder its viability for large-scale applications [18]. Another study by Ashraf[19] synthesized amide-modified biochar (ABC) through the pyrolysis of rice husk and achieved a Cr(VI) removal efficiency of 97% from a synthetic solution under optimized conditions (pH 2, 60 min, 2 g/L, 100 mg/L). Conversely, its functionalization depends on 1-1-[3-(trimethoxysilyl) propyl] urea, which is an expensive specialty organosilane and involves a multi-step synthesis process, potentially affecting its economic viability in industrial applications [19]. Moreover, Raji[20] explored fruit peel-based biosorbents (pumpkin, yellow melon, banana, and watermelon peels), which demonstrated remarkable removal efficiency for Pb(II) ions, exceeding 98%. Admitted, several factors may restrict their practical application and long-term effectiveness: the lengthy equilibration time of up to three days, the relatively high dosage of biosorbent required for optimal removal, elevated concentrations of Pb(II), and the inherent variability, poor mechanical stability, and potential biodegradation associated with raw biomass [20]. Therefore, chemical modification of agro-biomass derived biochar with inorganic chemicals/compounds, such as $FeSO_4.7H_2O$, Ni/Al-LDH, $ZnCl_2$, $Fe_3O_4$, $MgCl_2$ and MgO, may offer effective solutions for industries to mitigate toxicants in their wastewater [21].

For instance, a study by Tichem [22] investigated iron-modified rice husk biochar for removing Pb(II) ions, achieved removal efficiencies of 88.90% to 99.56% with diverse adsorbent dosages in simulated wastewater. Although these results are promising, high iron requirements (20:1 i.e., $FeSO_4.7H_2O$-to-biochar ratio) and potential regeneration challenges restrict its usage for industrial applications [22]. Similarly, another study on Ni/Al-layered double hydroxides loaded with rice husk-derived activated carbon achieved 82% Pb(II) removal (with initial 50 mg/L concentration solution). However, this modification relies on expensive chemicals like aluminium

nitrate, nickel nitrate and magnesium nitrate, posing potential supply chain challenges. Additionally, the co-precipitation technique requires prolonged reaction times, which complicates reproducibility [23]. Moreover, the exploration of activating agents has led to the development of $ZnCl_2$-impregnated banana peel and corncob biochar (1:1), achieving effective Cr(VI) removal, i.e., 98%, from synthetic solution. However, the study was limited to the removal of Cr(VI) i.e., a single metal ion, and the highly corrosive properties of $ZnCl_2$ (8%) raise safety concerns that may outweigh its benefits in eliminating multiple heavy metal ions from wastewater [24]. Another investigation used $Fe_3O_4$ nanoparticles modified with branched polyethyleneimine, and biochar derived from banana peels (BPB/$Fe_3O_4$/BPEI), achieving a remarkable 99.46% removal of Cu(II) ions [25]. Notably, the material's stability may be compromised due to Fe leaching during acid-mediated desorption. In a related study, Jain [26] developed a $Fe_3O_4$/AC nanocomposite from sunflower waste biomass for the removal of Cr(VI), Cu(II), and Cd(II), achieving maximum removal efficiencies of 95.3% at pH 2.0, 85.6%, and 96.5% at pH 6.0, respectively [26]. In accordance, little is known about utilization of non-magnetic coated co-pyrolyzed biochar obtained from agro-biomasses and its potential in removing metal ions from industrial wastewater. Moreover, most of the previous studies were restricted to removing single metal ions under controlled conditions, which necessitates testing of indigenously available materials in eliminating targeted metal ions from a competitive environment. Therefore, applying a non-magnetic coating on agro-biomass based biochar with consideration of enhanced active sites for targeted contaminants may provide an eco-friendly solution to enhance its commercial viability.

In lieu, Mg-loaded biochars present a safer and improved alternative for metal ions removal from wastewater. In this context, Lukman [27] reported that MgO-modified rice husk ash (MgO-RHA) achieved removal efficiencies of up to 79.20% for Cr(VI) and 96.02% for Pb(II), while

retaining above 75% and 68% removal, respectively, after three adsorption–desorption cycles, indicating excellent reusability and structural stability. However, the absence of detailed post-adsorption characterization limited understanding of the underlying mechanism, which restricts its practical utilization [27]. Another study has reported the impressive removal capacities for Cd(II) and Cu(II) by magnesium aluminium layered double hydroxide rice husk biochar composite (MgAl–LDH@RHB) in single-solute systems, reaching 125.34 and 104.34 mg/g through mechanisms of surface precipitation and ion exchange. Still, the lack of characterization of intermediate products (e.g., Al@RHB), which might provide valuable insights into the synthesis process, and the focus on single-solute systems leave the simultaneous removal of Cd(II) and Cu(II) unexplored [28]. Moreover, MgO-modified rice husk biochar has previously shown promising results in removing Cd(II), Cu(II), Zn(II) and Cr(VI), from quaternary systems, indicating higher adsorption capacities 105, 173, 104, and 47 mg/g, respectively [29]. Hence, previous research indicates the potential of MgO modified biochars in eliminating heavy metal ions from complex environments. Since, due to their technical limitations, scalability, affordability, and workability in environmentally relevant conditions, further research is needed to bridge current research gaps to enhance industrial capability, particularly tanneries to deal with their wastewater effluents. Therefore, the primary objectives of this study are to: 1) synthesize and characterize MgO-impregnated biochar derived from the co-pyrolysis of banana peels and rice husks, 2) investigate its adsorption potential and mechanisms for Pb(II) and Cr(VI) removal from single and binary solute systems, and 3) provide deep insights on the fate, mobility and adsorption behavior of targeted heavy metal ions from heterogeneous wastewater environments.

## 2. Materials and methods

### 2.1. Synthesis of raw and MgO modified biochar

Banana peels and rice husks were both locally sourced from Punjab, Pakistan, and preprocessed. Reagent-grade chemicals were obtained from Sigma-Aldrich (USA). The details are provided in Section S1.1. While three distinct types of raw biochars (RBCs) including rice husk biochar (RHBC), banana peel biochar (BPBC) and combined biochar (CBC) were initially produced using a pyrolysis reactor. This was achieved by placing rice husks powder (RHP), banana peels powder (BPP) and a 1:1 combination of RHP and BPP into a pyrolysis reactor under a nitrogen atmosphere, with a controlled flow rate of 200 mL/min at 550°C for 3 hours. Additionally, nitrogen purging was ensured for 20 minutes at a rate of 500 mL/min before and after the experiment [30]. Furthermore, all three types of RBCs were sieved through a 325-mesh filter (0.04 mm) and were stored in a zip-lock bag. The yields of biochar, biooil and biogas were also determined for each material (Section S2.1). Previous studies have shown that integrating magnesium oxide (MgO) into biochar enhances its adsorption capacity, electrostatic attraction and affinity for heavy metal contaminants and anionic pollutants in wastewater, through synergistic effects that increase surface area, active sites and modify surface charge properties [31]. Consequently, in current study, (30 g) RBC was activated using (40.66 g) magnesium chloride hexahydrate ($MgCl_2 \cdot 6H_2O$) in 0.2 L distilled water and was then allowed to stir for 24 hours. Afterwards, the mixture was subsequently dried in a hot air oven at a controlled temperature of 80°C for 24 hours. The resulting dried powder was then transferred into a pyrolysis reactor and was conducted under nitrogen purging environment: initially 20 minutes at 0.5 L/min, then 60 minutes at 400°C under 0.2 L/min during reaction time followed by 0.5 mL/min for 20 minutes at the end of reaction [32]. The solid residue obtained from this preparation process were identified

as magnesium oxide modified biochars (MgO@BCs) and designated as MgO@RHBC, MgO@BPBC and MgO@CBC, respectively.

## 2.2. Experimental conditions and procedure

To ascertain reliability and reproducibility, all batch adsorption experiments were conducted in duplicate, and the average values with relative standard deviations were reported for Cr(VI) and Pb(II) removal in both single and binary solute systems. Initially, the effects of varying doses (1, 2, 4 g/L) of six materials (RBCs and MgO@BCs) were examined in 100 mL volumes of 20 mg/L single-solute synthetic solutions (Pb(II) and Cr(VI)) at pH 2 and 4, with 2 hours of stirring at 180 RPM using an orbital shaker. Afterwards, based on superior adsorption performance, the most suitable MgO@BC was selected and used for subsequent adsorption experiments. Concentration experiments were conducted by varying initial metal ion concentrations from 10 to 100 mg/L in single and binary solute systems at pH (2, 4), using selected MgO@BC dosages (2 g/L, 4 g/L) with a contact time of 2 hours. This contact time has been extensively reported in the literature as adequate to achieve adsorption equilibrium and evaluate the adsorption capacity of MgO-modified biochar systems [33]. Regeneration studies of MgO@CBC in single-solute system (Cr(VI) at pH 2, Pb(II) at pH 4) and binary-solute system (at pH 2 only) were carried out at optimized conditions (initial metals ions concentration: 20 mg/L, dosage: 2 g/L). The adsorbent was then regenerated by dispersing spent MgO@CBC in 100 mL of 1 M NaOH solution, shaken for 2 hours to desorb metals ions from surface, followed by vacuum filtration and oven drying at 60°C for 4 hours, and then reused for the next successive cycle. At the end of each adsorption experiment, the aliquot was filtered using a 0.22 μm membrane filter and then analyzed for metal ion concentration. The solution preparation procedures are outlined in Section S1.4.

A calibration curve for chromium Cr(VI) with solutions of different concentrations (0.1-2 mg/L) yields an $R^2$ value of 0.999. Its detection involved preparing a reagent solution by dissolving 0.5 g of 1,5-diphenylcarbazide in 100 mL of acetone solution, adding 2 mL to 100 mL of filtrate, and analyzing using an Ultraviolet-Visible (UV-Vis) spectrophotometer (SPECORD 200) at a wavelength of 540 nm. A Pb(II) calibration curve was also prepared using various Pb(II) concentrations ranging from 0.05 to 5 mg/L, resulting in an $R^2$ value of 0.998. It was detected by mixing 3.5 mL of (0.05 to 5 mg/L) Pb(II) solution with 1 mL of 4 mM HCl, 4 mL of 0.3 M cetyltrimethylammonium bromide (CTAB), and 1.5 mL of 0.195 mM dithizone solutions, and analyzing using the spectrophotometer at a wavelength of 500 nm (Section S1.3). Removal efficiencies (%) and adsorption capacities ($q_e$) were quantified using Eq. (1, 2).

$$\text{Removal (\%)} = \frac{(Co-Ce)}{Co} \times 100 \quad (1)$$

$$q_e = \frac{(Co-Ce)x\ V}{m} \quad (2)$$

Ce and $C_0$ represent the final and initial concentrations of metal ions (mg/L) in the solutions, respectively. Also, m denotes the mass of the adsorbent (g) and V represents the initial volume of the suspension (L).



## 2.3. Analytical methods

Potentiometric titration (Section S1.3) was employed to determine the point of zero charge (pHpzc) values for RBCs and MgO@BCs. SEM-EDX (JSM-6490A, JEOL, Japan) was used to analyze the surface morphology and elemental composition of RBCs and MgO@BCs (before adsorption only). FTIR spectroscopy (Spectrum 100, PerkinElmer, Singapore) was used to identify chemical functional groups, and XRD analysis (Bruker D8 Advanced, Germany) was employed

to determine the crystallographic structure of RBCs and MgO@BCs, both before and after adsorption. BET analysis (Micromeritics Instrument Corp., USA) was used to measure specific surface area, pore volume and pore radius of RBCs and MgO@BCs (before adsorption only). The proximate analysis of RBCs and MgO@BCs was carried out in accordance with ASTM standard methods (ASTM E871-82, E872-82, and D3175-11) utilizing an oven and muffle furnace (Details are provided in Section S2.2). The degree of crystallinity was calculated using Eq. 3.

$$Xc = \frac{Ac}{Ac+Aa} \quad (3)$$

Where Ac represents the region under crystalline diffraction patterns and Aa represents the area under amorphous diffraction patterns. The crystallite size calculated using the Debye-Scherrer equation (Eq. 4).

$$D = \frac{K\lambda}{\beta \cos\theta B} \quad (4)$$

The Debye-Scherrer equation parameters defined as follows: crystallite size (D, nm), shape constant (K, assumed to be 0.9), X-ray wavelength (λ=0.15406 nm), peak breadth at half maximum height (β, radians), and reflection angle ($\theta_B$).



## 2.4. Isotherm models

The fitting performance of the nonlinearized Langmuir and Freundlich isotherm models was assessed using Eqs. 5 and 6 [34]. The parameters include: qe (mg/g), the equilibrium adsorption capacity representing the amount of Cr(VI) and Pb(II) adsorbed onto MgO@CBC surface sites at equilibrium; Ce (mg/L), the equilibrium residual concentration in solution; qm (mg/g), the theoretical maximum monolayer adsorption capacity; $K_L$ (L/mg), the Langmuir affinity constant indicative of adsorption energy; $K_F$, the Freundlich capacity coefficient; and n, the Freundlich heterogeneity factor characterizing the degree of surface heterogeneity.

$$qe = \frac{q_m K_L C_e}{1+KC_e} \quad (5)$$

$$qe = K_F C_e^{(1/n)} \quad (6)$$

# 3. Results and discussion

## 3.1. Characterization of raw and MgO modified biochar

### 3.1.1. SEM-EDX analysis

SEM images were employed to analyze the surface morphology and topographical features of RBCs and MgO@BCs. Fig. 1(A) reveals that RHBC possesses a moderately rough surface, consisting of interconnected macro particles due to excess silica content [35]. While the MgO@RHBC composite surface (Fig. 1(B)) displays irregularly shaped agglomerates, featuring

elevated particle density [36]. As shown in Fig. 1(C), BPBC exhibits irregular compressed porous

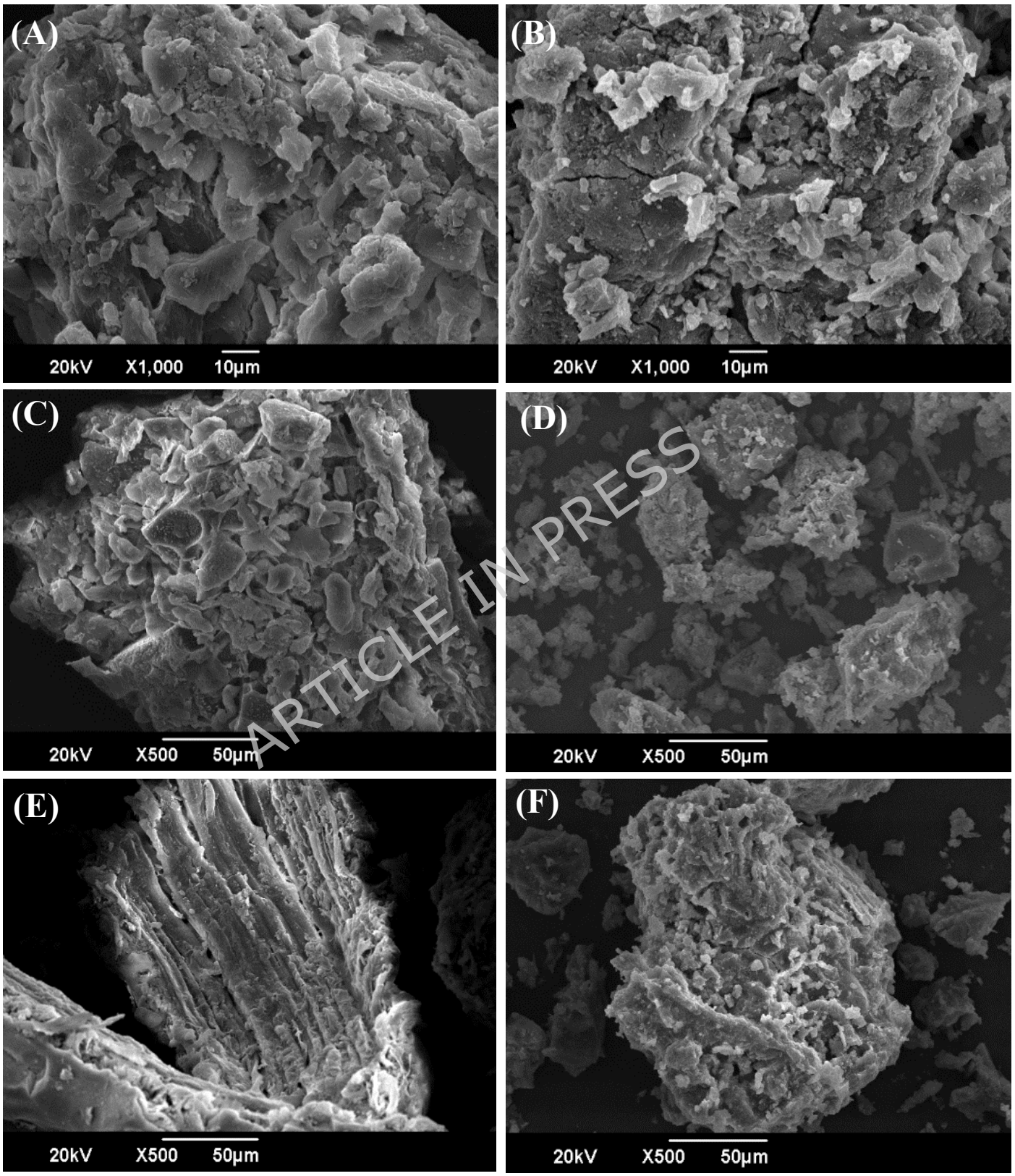


Fig. 1: SEM images (A) RHBC, (B) BPBC, (C) CBC, (D) MgO@RHBC, (E) MgO@BPBC, (F) MgO@CBC.

fragments, whereas MgO@BPBC demonstrates a mesh-structured surface texture with uneven MgO dispersion (Fig. 1(D)) [25]. Such observation was supported by EDX data, which confirmed the complete removal of silica from BPBC upon MgO modification, thus resulting in separated and mesh-structured particles (Section S2.3). Moreover, CBC in Fig. 1(E) exhibits a network of interlinked long sheets/rods, likely due to the fibrous nature and vascular structures of biomasses [37] and excess (31.9%) silica content (Section S2.3). Conversely, MgO@CBC morphology indicates compressed aggregated mass with enhanced porosity (Fig. 1(F)). Accordingly, MgO modification significantly increased Mg content as: RHBC (0.3%) → MgO@RHBC (8.1%), BPBC (1.4%) → MgO@BPBC (8.6%), and CBC (0.7%) → MgO@CBC (8.8%). These SEM-EDX results confirm the successful MgO loading onto BC surface, which might enhance the contaminant removal performance of synthesized BCs from wastewater.

**3.1.2. FT-IR analysis**

The FTIR spectra of RBCs (Fig. 2(A)) and MgO@BCs (Fig. 2(B)) were analyzed with a spectral range of 400-4000 $cm^{-1}$. Characteristically, the appearance of –OH stretching vibration around 3407-3428 $cm^{-1}$ confirms the presence of residual moisture in the analyzed adsorbents [38]. Specifically, in BPBC, peaks at 1023 and 1384 $cm^{-1}$ are attributed to the stretching vibrations of C–O–C/C–H, and O–C=O/$CO_3^{2-}$ bands which may enhance its performance during adsorption [39]. However, after modification to MgO@BPBC, the intensity of 1384 $cm^{-1}$ peak decreased significantly, thus indicating transformation of $CO_3^{2-}$ group to other forms [40]. Meanwhile, MgO@RHBC showed higher peak intensity at 3407 $cm^{-1}$ compared to RHBC, suggesting improved surface hydroxyl functionality after modification [41]. Furthermore, both RBCs and MgO@BCs spectra display characteristic bands, including C=O, –COOH (oxygen-containing acidic functional groups), and C=C stretching from alkenes or aromatic rings around 1600 $cm^{-1}$,

which may facilitate adsorption of targeted metal ions. However, upon modification with MgO, the intensity of these bands increased, indicating an enhancement in carbonization [41]. Specifically, the peaks previously measured at 1613 $cm^{-1}$ for RHBC, 1628 $cm^{-1}$ for BPBC, and 1620 $cm^{-1}$ for CBC shifted to 1637, 1635, and 1635 $cm^{-1}$, respectively, after MgO modification. This observed shift suggests possible coordination between Mg species and the oxygen-rich surface functional groups, confirming the potential impact of the modification [42]. Notably, the presence of silanol (Si–OH) and siloxane (Si–O–Si–OH) groups in RBCs was confirmed by peaks at 1095, 801, and 465 $cm^{-1}$ (RHBC) and 792 and 463 $cm^{-1}$ (CBC) [43]. However, these groups are chemically inert and non-reactive, which is consistent with previous findings [44]. Furthermore, in CBC, the Si–O–Si stretching peak shifted from 1037 to 1111 $cm^{-1}$ following MgO modification. This observation suggests an interaction between Mg species and Si functional groups, potentially through the formation of Si–O–Mg linkages. Moreover, the formation of a cubic $Mg_2Si$ structure in MgO@CBC, as confirmed by XRD analysis, further indicates that silica groups actively participate in creating potential active sites for adsorption [45]. Following modification, the MgO@BCs spectra exhibited distinct band of Mg–O functional groups: MgO@RHBC (725, 619, and 467 $cm^{-1}$), MgO@BPBC (623 $cm^{-1}$), and MgO@CBC (622 and 492 $cm^{-1}$) [46]. In general, the FT-IR analysis clarified the variation in bonding features of RBC and MgO@BCs.

### 3.1.3. XRD analysis

The crystal structure of RBCs and MgO@BCs was investigated using XRD analysis as presented in Fig 2 (C, D) with a 2θ range of 10-80°. In RHBC, peaks at 26.32° (005) and 26.4° (002) indicated hexagonal SiC and C structures respectively, consistent with PDF# 42-1360, and 41-1487, which confirmed the predominant amorphous carbon composition [47]. The significant presence of silica was highlighted by a prominent peak at 26.15° (101), corresponding to PDF#

11-0252, indicating high quartz content, which was also evidenced by EDX analysis [48]. In BPBC, broad peaks at 40.38° (520) and 28.11° (006) were observed, indicating the presence of cubic fullerite C60 and hexagonal iron carbide $Fe_3C_8$ structures, which matched PDF# 49-1720

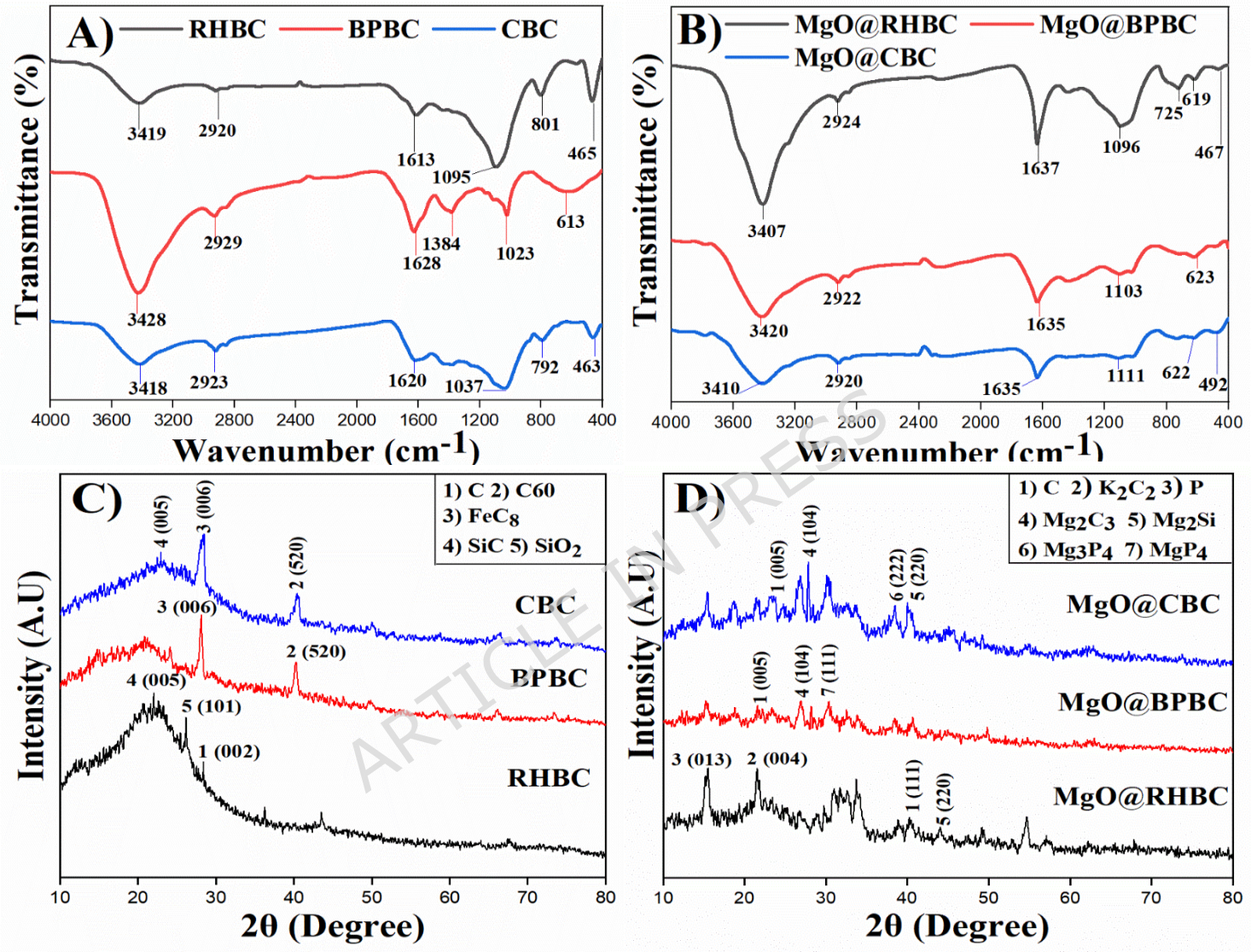


Fig. 2: FTIR and XRD analysis: (A, C) RBCs; (B, D) MgO@BCs.

and 51-0624, respectively [39]. CBC exhibited peaks at 28.11° (006) and 26.32° (005), confirming the presence of hexagonal $Fe_3C_8$ and SiC structures, consistent with PDF# 51-0624 and 42-1360.

Distinct MgO peaks were observed after RBCs modification, confirming successful coating [49]. MgO@RHBC exhibited a distinct diffraction peak at 39.98° (220), indicative of a

cubic $Mg_2Si$ structure, matching PDF# 35-0773 [50]. MgO@BPBC exhibited peaks at 27.43° (104) and 32.49° (111), indicative of hexagonal $Mg_2C_3$ and monoclinic $MgP_4$ structures, corresponding to PDF# 01-1138 and 300795, respectively. MgO@CBC exhibited peaks at 39.98° (220) and 37.74° (222), indicative of cubic $Mg_2Si$ and $Mg_3P_2$ structures (PDF# 35-0773 and 04-0489) [51]. However, the absence of distinct characteristic peaks associated with MgO in the MgO@BC composite indicates the presence of poorly crystalline or highly dispersed MgO phases. This phenomenon may result from the uniform distribution of Mg species throughout the biochar matrix and their interactions with the inherent mineral constituents during pyrolysis. These interactions could potentially lead to the formation of secondary Mg-based crystalline phases. The crystallite sizes of the RHBC, BPBC and CBC were 0.37, 0.30, and 0.24 nm, respectively. After modification, they increased to 0.85, 3.52, and 0.99 nm for MgO@RHBC, MgO@BPBC and MgO@CBC. The degree of crystallinity also increased significantly after modification, rising from 3.05% to 9.44% for RHBC, 4.81% to 16.72% for BPBC, and 6.85% to 15.51% for CBC. These XRD analysis suggest that the emergence of new surface sites and the presence of multiple pyrolytic components in MgO@BCs may enhance their adsorption performance for contaminants from wastewater.



**3.1.4. BET analysis**

As shown in Table 1, BET analysis revealed distinct changes in surface properties of MgO@BCs compared to RBCs. The surface area of RBCs was found to be 12.07 $m^2/g$ (RHBC), 0.73 $m^2/g$ (BPBC), and 7.03 $m^2/g$ (CBC). In comparison, MgO modification resulted in variable changes in surface area across different BCs, specifically in MgO@BPBC (10.19 $m^2/g$) and MgO@CBC (8.93 $m^2/g$) with MgO@BPBC exhibiting a remarkable 14-fold increase. The increase in the surface area of MgO@BPBC can be attributed to Mg-assisted activation, which

facilitated extensive pore generation during pyrolysis [52]. Additionally, the intrinsic composition and structural characteristics of BP biomass likely played a role in forming a highly porous carbon framework. However, the decrease (~8%) in surface area of MgO@RHBC (11.12 $m^2/g$) compared to RHBC (12.07 $m^2/g$) can be attributed to the deposition of MgO within the pore structure, leading to partial pore blockage and reduced accessibility of internal surfaces. This behavior is consistent

| Parameters | Types of Material | | | | | |
|---|---|---|---|---|---|---|
| | RHBC | BPBC | CBC | MgO@RHBC | MgO@BPBC | MgO@CBC |
| BET Surface Area ($m^2/g$) | 12.07 | 0.73 | 7.03 | 11.12 | 10.19 | 8.93 |
| Pore Volume ($m^3/g$) | 0.002 | 0.0001 | 0.002 | 0.003 | 0.002 | 0.003 |
| Pore Radius (nm) | 2.03 | 2.05 | 2.03 | 2.06 | 2.05 | 2.06 |

**Table 1:** Physical properties of RBCs and MgO@BCs.

with previous studies, where metal oxide loading onto BC has been reported to reduce surface area due to pore obstruction effects [53]. In addition, MgO@BC showed a marginal to moderate increase in pore volume and negligible

increase in pore radius compared to RBCs. In general, these detailed surface features of synthesized BCs might be helpful in evaluating their adsorption performance for targeted metal ions, such as Cr(VI) and Pb(II) from wastewater.

## 3.2. Batch adsorption study

### 3.2.1. Influence of pH and dosage

Importantly, due to the presence of oxygen-containing acidic functional groups, as confirmed from FT-IR analysis, both RBCs and MgO@BCs surface functional groups and active sites exhibit pH-dependent sensitivity, which influence their adsorption performance [54]. Notably, the pHpzc values of RBCs and MgO@BCs were determined to be RHBC (5.83), MgO@RHBC (9.67), BPBC (7.69), MgO@BPBC (9.55), CBC (9.04), and MgO@CBC (9.65)

(Section S2.4). Nevertheless, the determined pHpzc values exceed the pH levels (2, 4) used in the current study. At pH values below the pHpzc, protonation of biochar functional groups occurs ($^{-}OH + H^{+} \rightarrow {}^{-}OH_2^{+}$), resulting in a net positive surface charge under acidic conditions. This phenomenon enhances the sorption capacity of biochar towards anionic metal species [55]. Consistent with this finding, Cr(VI) removal was significantly enhanced at pH 2 compared to pH 4 when a comparative study of RBCs and MgO@BCs was conducted, as shown in Fig. 3 (A, B) [56]. This enhanced performance can be attributed to the predominance of anionic Cr(VI), namely $HCrO_4^-$ and $CrO_4^{2-}$, which facilitate stronger electrostatic interactions with the positively charged BCs surface [57]. Conversely, at pH 4, the reduced $H^+$ ions and increased $OH^-$ ions facilitate competition among anionic Cr(VI) species for surface binding sites, ultimately decreasing removal efficiency [4]. As shown in Fig. 4(A), substantially higher Cr(VI) adsorption performance (73.6%, 7.36 mg/g) than RHBC (42.7%, 4.27 mg/g) was observed at 2g/L dosage. Particularly, CBC exhibited a moderate Cr(VI) removal efficiency of 80.5% (8.05 mg/g), which was substantially enhanced to 94.3% (9.43 mg/g) due to highly reactive MgO functional groups in MgO@CBC. Moreover, a slight improvement in adsorption performance of MgO@BPBC (97%, 9.7 mg/g) than

BPBC (95.8%, 9.58 mg/g) was observed. Such observations may be linked to the provision of more active sites and facilitating MgO particle dispersion in MgO@BCs. Contrary to this, further increasing the dosage to 4 g/L resulted in a decrease in Cr(VI) adsorption performance of BPBC (69%), MgO@BPBC (68.4%), CBC (74%), and MgO@CBC (90%). This suggests that higher BC dosages may promote particle destabilization, aggregation, and site overlapping, which can reduce

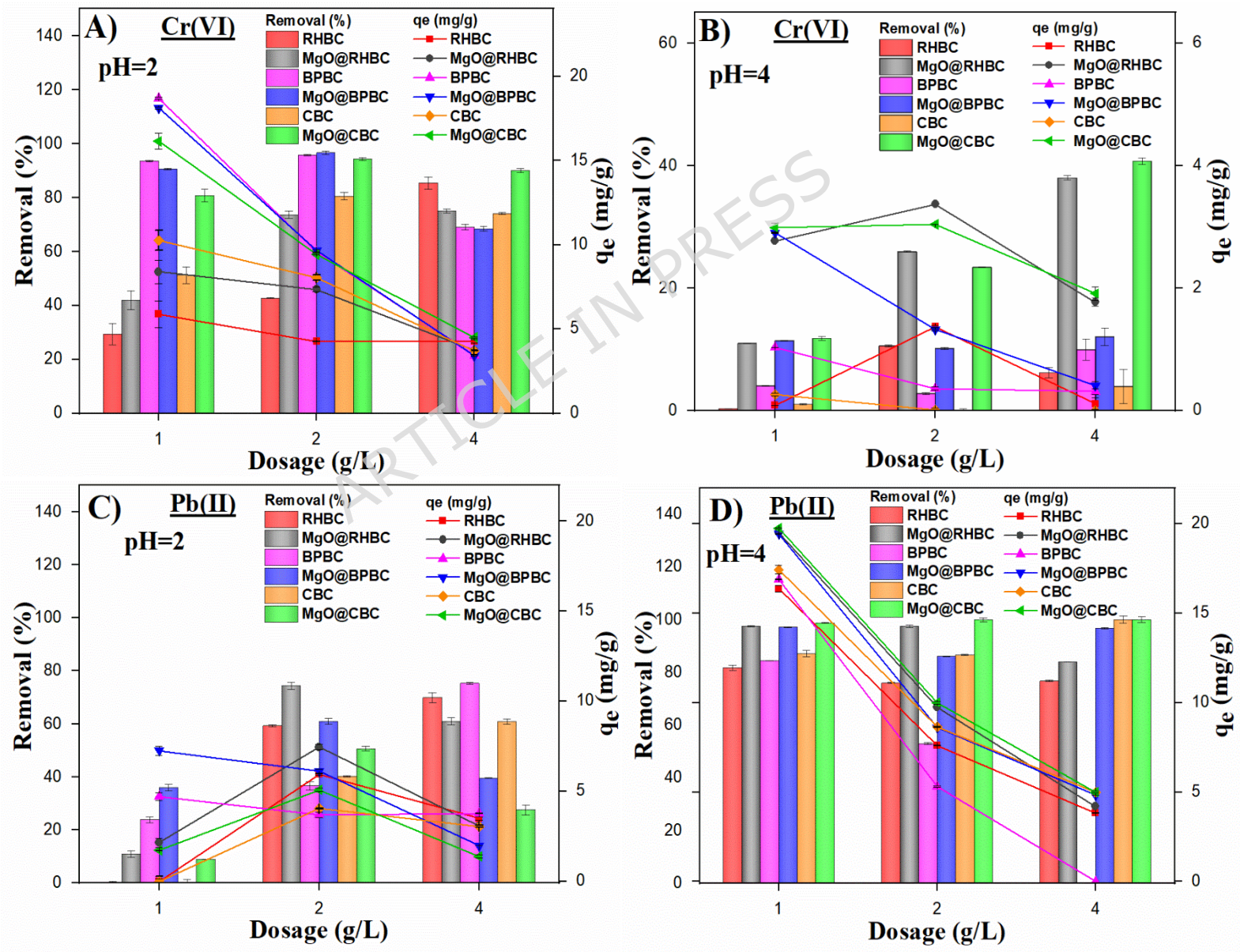


Fig. 3: Effect of dosages on Cr(VI) (A, B) and Pb(II) (C, D) removal (single solute, 20 mg/L concentration).

the effective surface area and accessibility of active sites, ultimately degrading its adsorption properties [58].

Contrary to Cr(VI) species, an opposite Pb(II) adsorption trend was observed, where higher removal was achieved at pH 4 (Fig. 3(D)) compared to pH 2 (Fig. 3(C)), which may be attributed to the abundance of cationic Pb(II) ions at pH 2 [34]. Meanwhile, at pH 4, Pb(II) removal was enhanced due to a relatively higher availability of $OH^-$ ion concentration, which facilitated better charge neutralization. Still, the effect of dosage indicated better Pb(II) adsorption performance of RBCs and MgO@BCs at 2 g/L than 4 g/L. For instance, at 2 g/L dosages, RBCs (RHBC, BPBC, and CBC) achieved removal efficiencies of 76%, 53%, and 87%, and sorption capacities of 7.60, 5.30, and 8.66 mg/g, respectively. MgO-modified counterparts showed improved removal performance (98%, 86%, and 100%) and capacities (9.75, 8.60, and 10 mg/g), respectively (Fig. 3(D)). Unlike Cr(VI) removal response, higher Pb (II) adsorption by RHBC was observed, which may be attributed to its pHpzc value of 5.83. The relatively small difference between solution pH and pHpzc may have reduced electrostatic repulsion and could have facilitated Pb(II) uptake through surface complexation with oxygen-containing functional groups. Although limited hydrolysis of Pb(II) to $Pb(OH)^+$ may occur under mildly acidic conditions, its contribution at pH 4 is expected to be minor because Pb(II) precipitation is negligible at this pH. In this case, Pb(II) removal was mainly governed by adsorption-related interactions rather than hydroxide precipitation [34]. In contrast, the removal efficiency of Pb(II) by BPBC at pH 4 exhibited a dosage-dependent decline, decreasing from 84.46% at 1 g/L to 50% at 2 g/L, and eventually becoming 0% at 4 g/L (Fig. 3(D)). This decline can be attributed to the intensified electrostatic repulsion between the positively charged BPBC surface (pHpzc (7.69)) and Pb(II) ions at higher dosages, which limited its adsorption capabilities [59]. Amongst all, MgO@CBC provided

consistent removal for Pb(II) at pH 4 and Cr(VI) at pH 2, attributable to the synergistic interplay of its dual properties. The high carbon content (41.33%) and silica-based structure of MgO@CBC, as confirmed by proximate analysis (Section S2.2) and spectroscopic characterization (FT-IR, XRD), enhanced its stability and adsorption properties. Consequently, MgO@CBC was selected for subsequent experiments to investigate its adsorptive exclusion potential of Cr(VI) and Pb(II) species from wastewater.

### 3.2.2. Influence of initial metal ion concentration

#### *3.2.2.1. Single solute system*

Fig. 4 (A, B) illustrates the concentration dependent removal of Cr(VI) in a single solute system at pH 2 and 4, using MgO@CBC dosages of 2 g/L and 4 g/L. As the initial Cr(VI) concentration increased from 10 to 100 mg/L, the removal efficiency decreased. At pH 2, the removal efficiency dropped from 96% to 48% (4.8 to 24.2 mg/g) with a 2 g/L dosage, and from 95% to 60% (2.37 to 15 mg/g) with a 4 g/L dosage. The increased removal at lower concentrations may be attributed to the abundance of adsorption sites and oxygen containing functional groups, including hydroxyl, phenol, and carboxyl [60]. Whereas, at pH 4, efficiency decreases from 30% (1.51 mg/g) to 0% for the 2 g/L dosage and from 80% to 5% (1.98 to 1.15 mg/g) for the 4 g/L dosage. This indicates that higher BCs applied dosages may improve adsorption performance by efficiently capturing targeted metal ions from wastewater.

Conversely, distinct dosage-dependent trends were observed in the removal of Pb(II) under similar conditions to Cr(VI). At 2 g/L, a notable decrease in removal upon increasing Pb(II) concentration (10 to 100 mg/L) was observed, from 55% to 12% (2.76 to 6.01 mg/g) at pH 2 and from 100% to 75% (5 to 37.5 mg/g) at pH 4 (Fig 4(C)). In contrast, at 4 g/L, the removal efficiency decreased significantly from 38% (0.95 mg/g) to 0% at pH 2, and from 100% to 22.85% (2.5 to 5.71 mg/g) at pH 4 (Fig 4(D)). The reduced removal at higher dosage (4 g/L) and pH 4 can be attributed to the enhanced cationic properties of MgO@CBC (pHpzc: 9.65), which may intensify

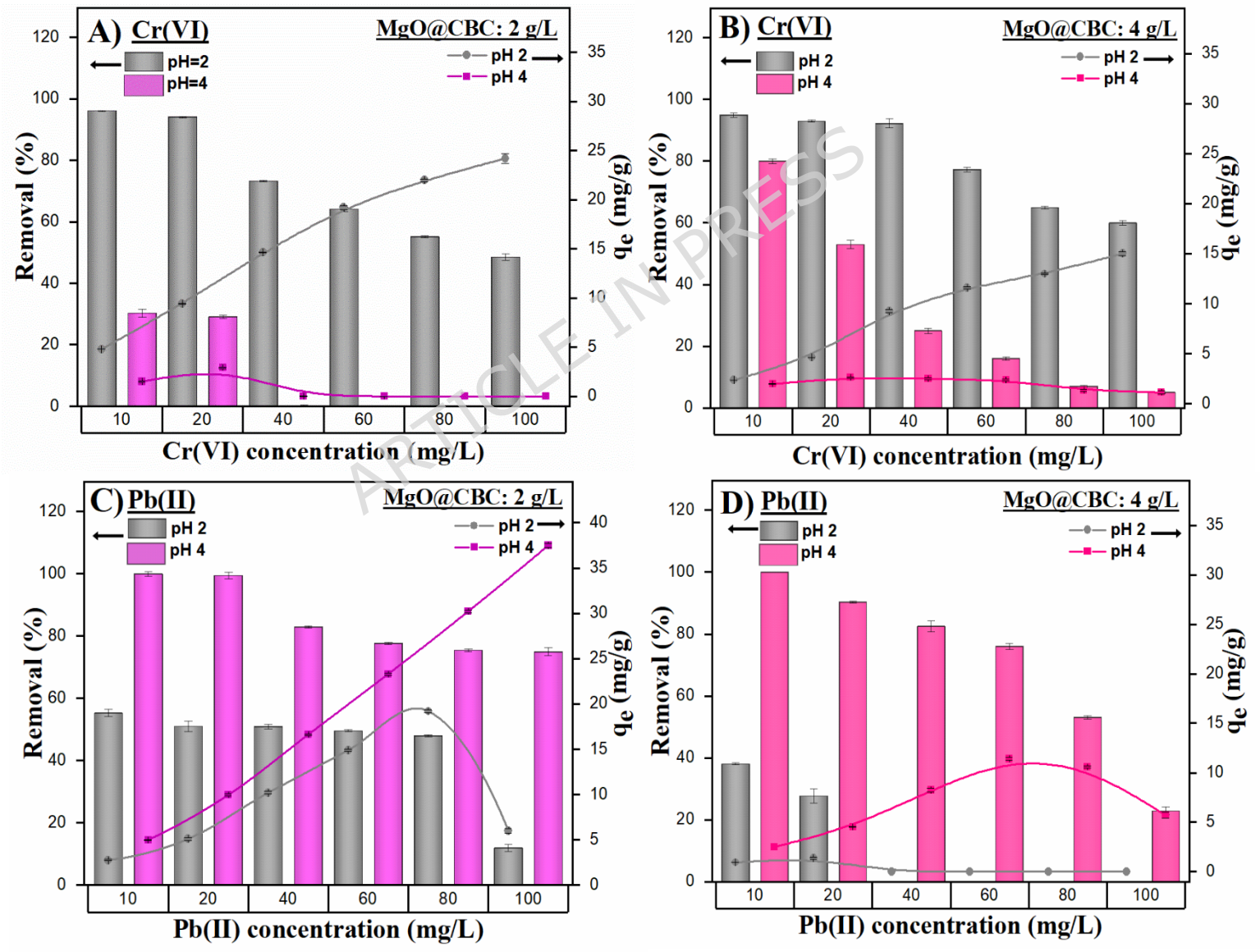


Fig. 4: Effect of concentration on Cr(VI) (A, B) and Pb(II) (C, D) removal (single solute).

the electrostatic repulsion between the adsorbent and $Pb^{2+}$ ions [61]. Therefore, such a drastic decline in removal efficiency at elevated Pb(II) concentrations (80 and 100 mg/L) was observed. In contrast, at a lower dosage (2 g/L), the cationic properties of MgO@CBC are attenuated, thereby facilitating enhanced interactions between the active surface sites and Pb(II) ions. This results in the formation of more stable complexes at 2 g/L, yielding higher removal efficiencies at elevated Pb(II) concentrations compared to 4 g/L. Therefore, it may be deduced from the above results that increasing adsorbent dosage may not be an influential factor in removing contaminants from wastewater, rather surface properties particularly surface potential is mainly responsible in the overall removal process [62]. Therefore, our study indicated that higher MgO@CBC dosages compromise Pb(II) removal performance, thereby retarding the efficiency of system.

### *3.2.2.2. Binary solute system*

Fig. 5 (A, B) illustrates the influence of Pb(II) ions onto Cr(VI) removal in a binary solute system under increasing metals ions concentration from 10 to 100 mg/L. At 2 g/L MgO@CBC dosage, Cr(VI) removal decreased from 95% to 61% (4.7 to 30.5 mg/g) at pH 2 and from 32% to

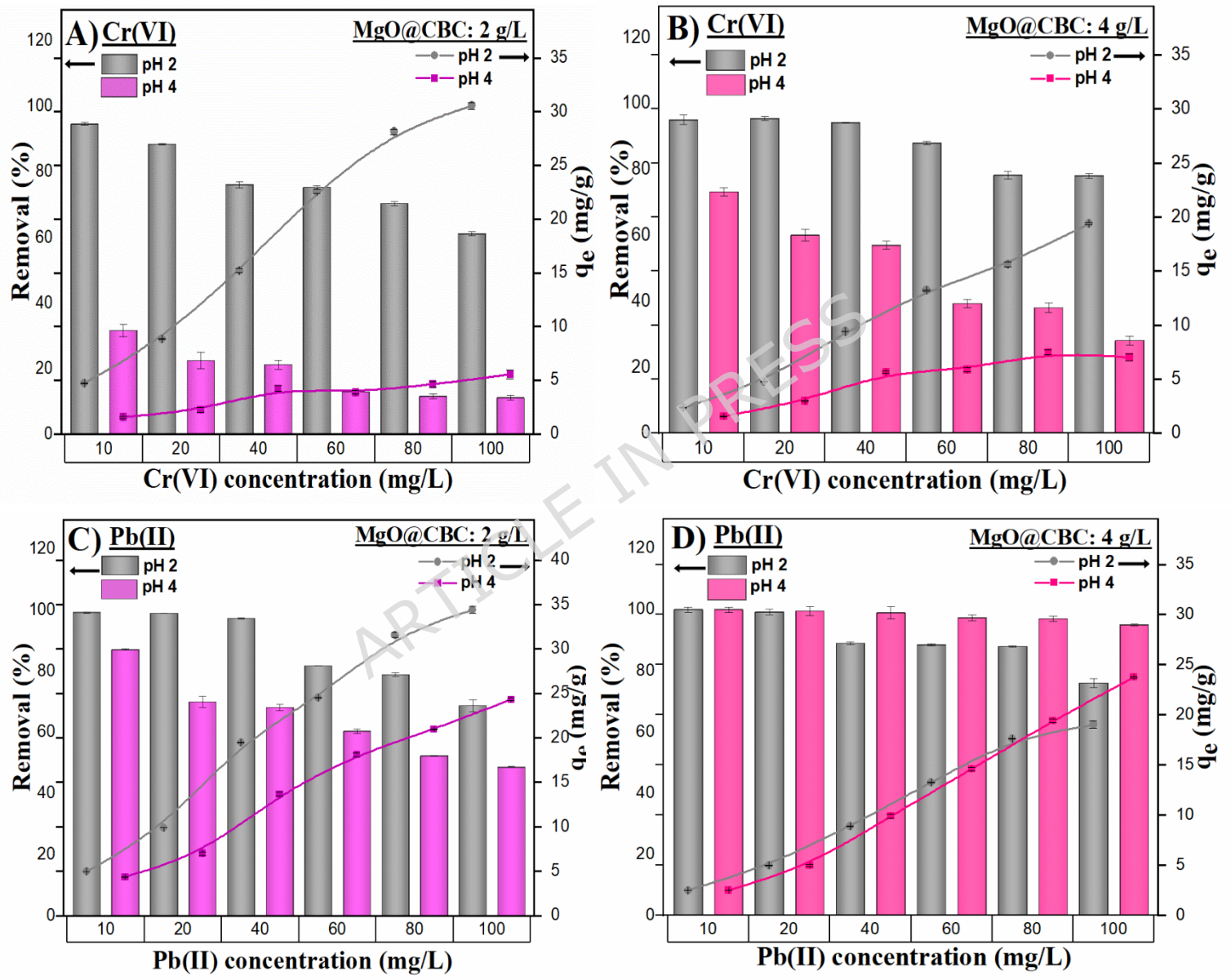


11% Fig. 5: Effect of concentration on Cr(VI) (A, B) and Pb(II) (C, D) removal (binary solute).

(1.5 to 5.5 mg/g) at pH 4 (Fig. 5(A)). A higher dosage of 4 g/L resulted in Cr(VI) removal trend as 95% to 78% (2.37 to 19.3 mg/g) at pH 2 and 73% to 28% (1.83 to 7 mg/g) at pH 4 (Fig. 5(B)).

Interestingly, it was observed that presence of Pb(II) ions facilitated Cr(VI) uptake by MgO@CBC, thus indicating the overall synergistic effect under higher contaminant loading conditions. Previously, synergistic adsorptive removal performance of metal ions under multicomponent environment has also been reported, where presence of one metal ions improved the efficiency of system in eliminating other distinct types of contaminants [63]. At the same time, such removal responses are a function of redox conditions and contaminant types. In accordance, current results also indicate a slight decline in Cr(VI) removal under low studied metals ions concentrations (10 to 20 mg/L), where the removal efficiency in the binary system (88.5%) was lower than that in the single system (94 %) at 2 g/L dosage. Under such an aqueous environment, competitive inhibitory effect might occr either due to availability of limited adsorption sites, less interaction with adsorbent surface or formation of stable surface complexes between metals ions and adsorbent [64], [65]. To examine the overall removal mechanism, further surface evaluation of spent MgO@CBC adsorbent has been presented in a subsequent section. Meanwhile, Pb(II) removal efficiency as shown in Fig. 5(C, D), decreased from 99% to 69% (4.9 to 34 mg/g) at pH 2, and from 87% to 48% (4.35-24 mg/g) at pH 4, at a dosage of 2 g/L and increasing metals ions concentration (10 to 100 mg/L) respectively (Fig. 5(C)). A higher dosage of 4 g/L resulted in removal efficiencies as 100% to 76% (2.5-19 mg/g) at pH 2, and 100% to 95% (2.5-23.75 mg/g) at pH 4 (Fig. 5(D)). In comparison to single solute system, Pb(II) removal performance with increasing metals concentrations declined from (100% to 75%) to (87% to 48%) at pH 4 and 2 g/L MgO@CBC dosage, which may be due to the competition with Cr(VI) species for active surface sites during removal process. Contrary to this, all other studied solution conditions indicated significant enhancement in Pb(II) removal in binary system than single solute system. For instance, at pH 2, dosage 4 g/L, and concentration of 100 mg/L, the removal efficiency increased from 0%

(single system) to 76% (binary system), while at pH 4, it improved from 22.85% (single system) to 95% (binary system), respectively. Such observation may be attributed to the co-attachment of dissolved metal complexes, likely resulting via interaction between positively charged $Pb^{2+}$ and negatively charged $CrO_4^{2-}$ and $HCrO_4^-$, onto MgO@CBC surface, thereby synergistically enhancing Pb(II) removal from wastewater [65]. In general, optimization of adsorption parameters in the binary system yielded maximum simultaneous removal efficiencies of 88.5% for Cr(VI) and 99% for Pb(II) at pH 2, 20 mg/L concentration, and 2 g/L dosage. This outcome suggests a synergistic removal effect, facilitated by cumulative adsorption and strengthened metal complex formation.

### 3.3. Adsorption isotherm

Fig. 6 and 7 illustrate the Langmuir and Freundlich isotherm plots for Cr(VI) and Pb(II) adsorption onto MgO@CBC in single and binary solute systems, respectively, with the

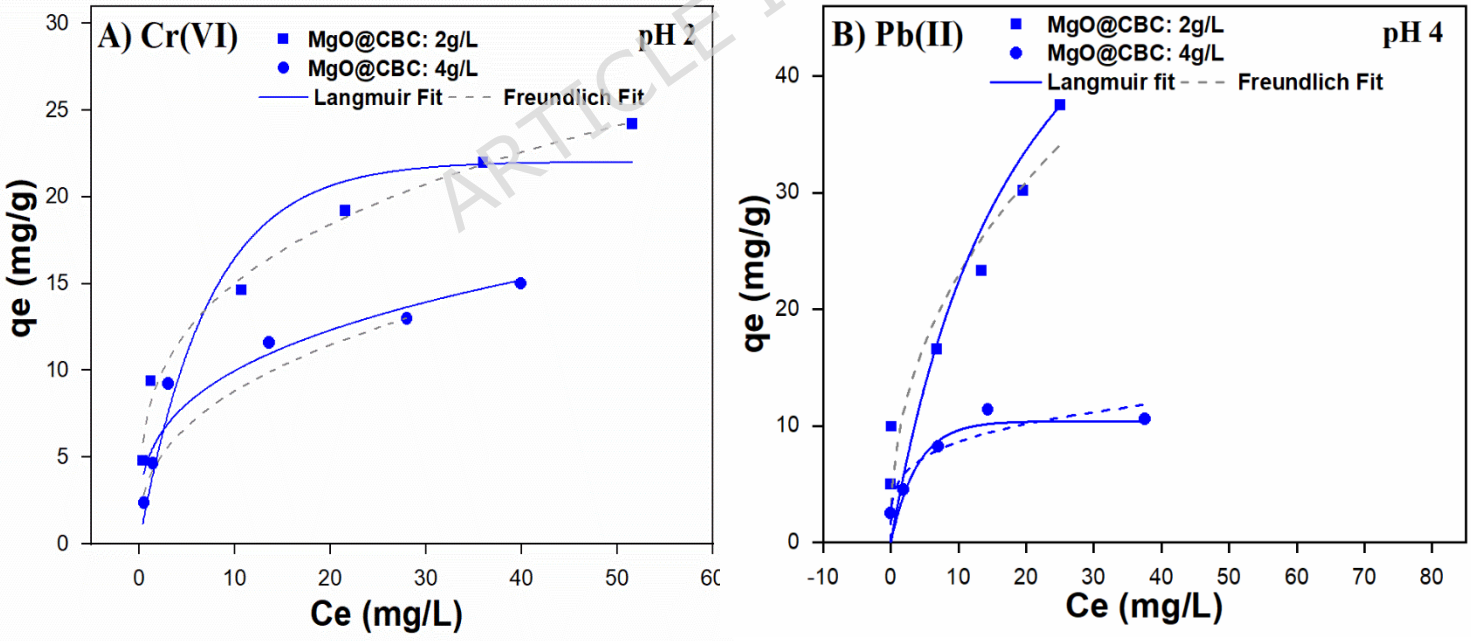


Fig. 6: Isotherm graphs (single solute): Cr(VI) A) pH 2; Pb(II) B) pH 4.

corresponding model parameters summarized in Table 2. In the single solute system (Fig. 6(A)), Cr(VI) at pH 2 exhibited a better fit to the Freundlich model, with $R^2$ values of 0.984 and 0.987 at

dosages of 2 g/L and 4 g/L, respectively, while the Langmuir model yielded $R^2$ values of 0.722 and 0.935 at the same dosages. For Pb(II) at pH 4 (Fig. 6(B)), neither model provided an adequate fit, with the Freundlich model yielding $R^2$ values of 0.837 and 0.695, and the Langmuir model yielding $R^2$ values of 0.712 and 0.748, at dosages of 2 g/L and 4 g/L, respectively. Similarly, neither model accurately described the Cr(VI) adsorption data at pH 4 and Pb(II) at pH 2, as evident from the scattered data points (graphs provided in Section S2.5), both likely to attribute pH-dependent removal behavior.

In the binary solute system, the Langmuir model for Cr(VI) yielded $R^2$ values of 0.937 and 0.989 at pH 2 (Fig. 7(A)), and 0.901 and 0.946 at pH 4 (Fig. 7(B)), at dosages of 2 g/L and 4 g/L, respectively. The Freundlich model yielded $R^2$ values of 0.966 and 0.939 at pH 2, and 0.985 and 0.983 at pH 4, at the same dosages, respectively. For Pb(II), the Langmuir model yielded $R^2$ values

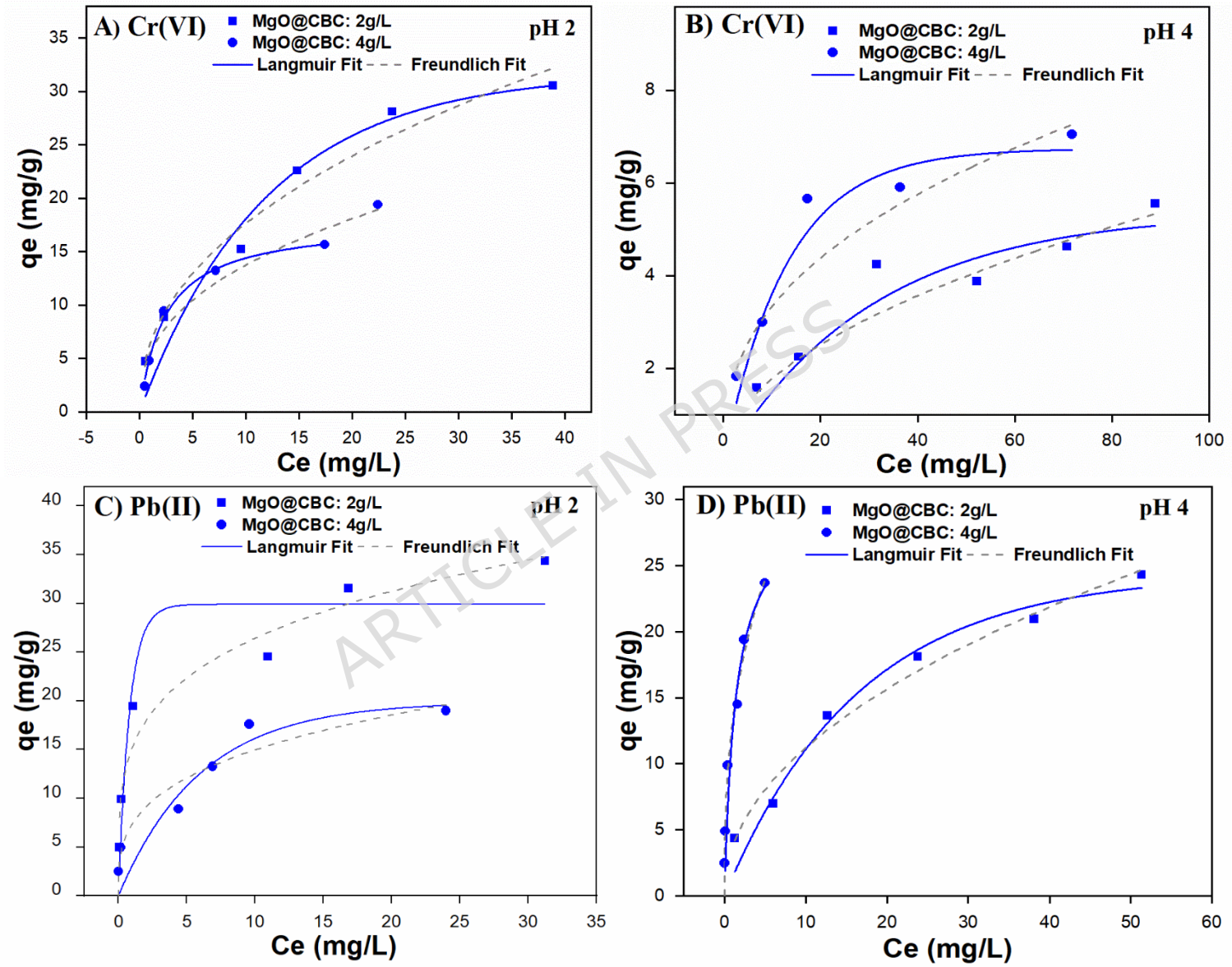


Fig. 7: Isotherm graphs (binary solute): Cr(VI) A) pH 2, B) pH 4; Pb(II) C) pH 2, D) pH 4.

of 0.862

and 0.825 at pH 2 (Fig. 7(C)), and 0.908 and 0.962 at pH 4 (Fig. 7(D)), at dosages of 2 g/L and 4 g/L, respectively. Whereas the Freundlich model yielded $R^2$ values of 0.936 and 0.874 at pH 2,

and 0.965 and 0.976 at pH 4, at the same dosages, respectively. An exception was observed for Cr(VI) at pH 2 and 4 g/L dosage, which exhibited a better fit to the Langmuir model, suggesting homogeneous monolayer adsorption driven by uniform surface site occupancy under competitive conditions, while all remaining conditions predominantly conformed to the Freundlich model, indicating heterogeneous multilayer adsorption behavior. Collectively, the higher $R^2$ values and improved model conformity observed in the binary system suggest that the simultaneous presence of Cr(VI) and Pb(II) promotes more organized and cooperative adsorption behavior on the MgO@CBC surface.

**Table 2:** Isotherm model parameters (MgO@CBC): single and binary system (Cr(VI) and Pb(II)).

| System | Metal | pH | Dosage (g/L) | Langmuir | | | Freundlich | | |
|---|---|---|---|---|---|---|---|---|---|
| | | | | $q_m$ (mg/g) | $k_L$ (L/mg) | $R^2$ | Kf (L/mg) | n | $R^2$ |
| Single | Cr(VI) | 2 | 2 | 22.02 | 0.137 | 0.722 | 7.65 | 3.41 | 0.984 |
| | | | 4 | 13.30 | 0.34 | 0.935 | 3.67 | 2.63 | 0.987 |
| | Pb(II) | 4 | 2 | 68.12 | 0.048 | 0.712 | 8.48 | 2.31 | 0.837 |
| | | | 4 | 10.41 | 0.257 | 0.748 | 4.98 | 4.20 | 0.695 |
| Binary | Cr(VI) | 2 | 2 | 31.745 | 0.084 | 0.937 | 6.36 | 2.25 | 0.966 |
| | | | 4 | 17.84 | 0.41 | 0.989 | 5.54 | 2.51 | 0.939 |
| | | 4 | 2 | 5.38 | 0.032 | 0.901 | 0.553 | 1.98 | 0.985 |
| | | | 4 | 6.73 | 0.076 | 0.946 | 1.33 | 2.53 | 0.983 |
| | Pb(II) | 2 | 2 | 29.88 | 1.22 | 0.862 | 15.16 | 4.14 | 0.936 |
| | | | 4 | 19.88 | 0.167 | 0.825 | 7.36 | 3.24 | 0.874 |
| | | 4 | 2 | 30.04 | 0.708 | 0.908 | 13.14 | 2.66 | 0.965 |
| | | | 4 | 24.41 | 0.06 | 0.962 | 3.69 | 2.07 | 0.976 |

### 3.4. Removal mechanism

Current batch-mode Cr(VI) and Pb(II) adsorption investigations using MgO@CBC in both single and binary solute systems provided detailed mechanistic insights into removal behavior of both species. Further mechanistic validations were conducted through spectroscopic analysis (FT-IR and XRD) of spent MgO@CBC (Fig. 8 (A, B) and (C, D)). For instance, the C=O/C=C functional group at 1635 $cm^{-1}$ in MgO@CBC exhibited noticeable band shifts after adsorption. Specifically, at pH 2 (Fig. 8(A)), the peak shifted to 1610 $cm^{-1}$ for AR:MgO@$CBC_{Cr}$ (Cr adsorbed

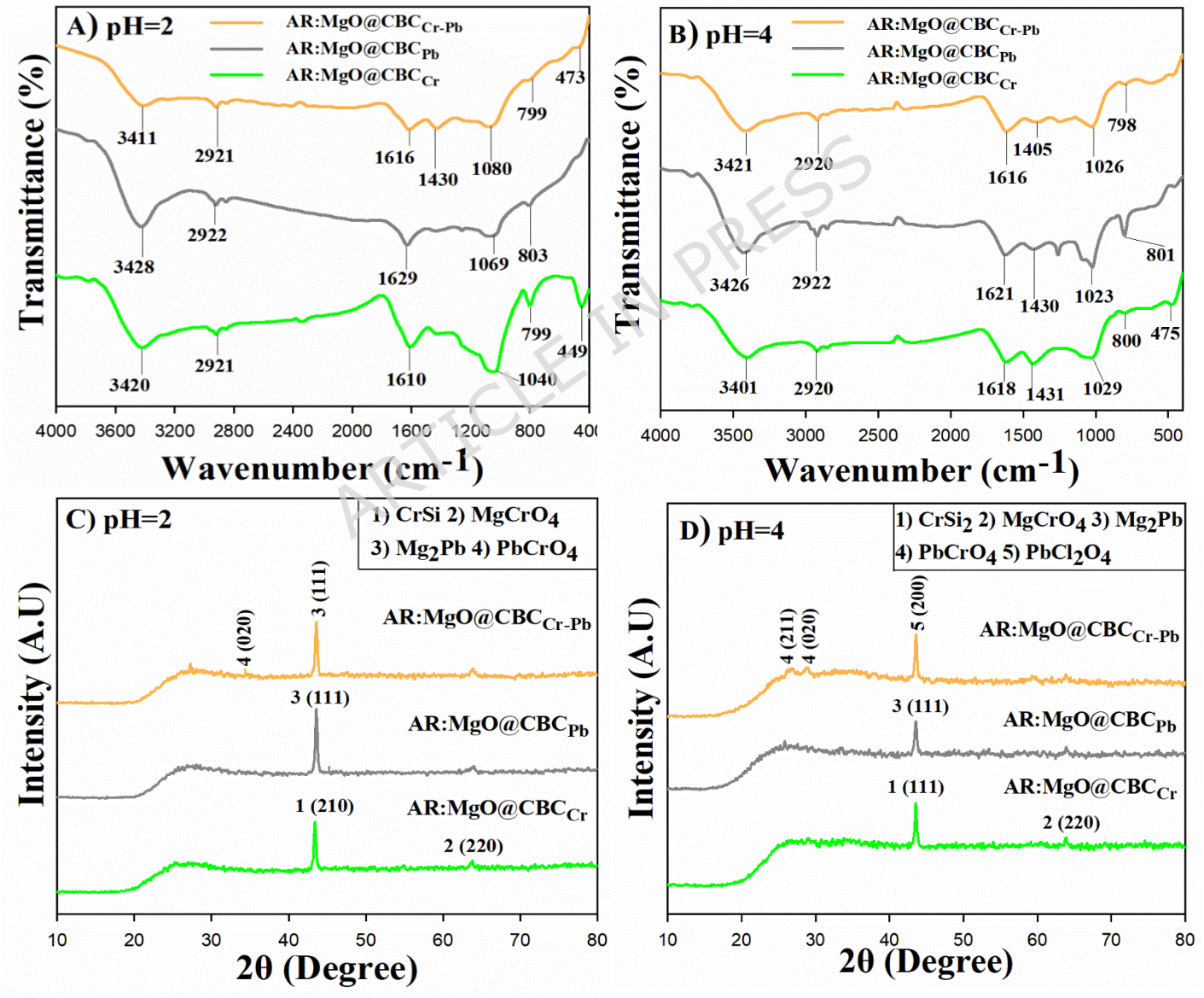


Fig. 8: FTIR (A, B) and XRD (C, D) analysis of spent MgO@CBC.

MgO@CBC), 1629 $cm^{-1}$ for AR:MgO@$CBC_{Pb}$ (Pb adsorbed MgO@CBC), and 1616 $cm^{-1}$ for AR:MgO@$CBC_{Cr–Pb}$ (Cr and Pb adsorbed MgO@CBC). At pH 4 (Fig. 8(B)), shifts were observed at 1618 $cm^{-1}$ for AR:MgO@$CBC_{Cr}$, 1621 $cm^{-1}$ for AR:MgO@$CBC_{Pb}$, and 1616 $cm^{-1}$ for AR:MgO@$CBC_{Cr–Pb}$. In addition, the O–H stretching vibration at 3410 $cm^{-1}$ in MgO@CBC exhibited variations in band intensity after adsorption across all studied systems, indicating the collective involvement of oxygen-containing functional groups in the adsorption process, which remains consistent across different pH conditions [66]. Furthermore, the Si–O–Si stretching vibration, initially recorded at 1111 $cm^{-1}$ in MgO@CBC, shifted to lower wave numbers (1023–1080 $cm^{-1}$) in all investigated systems at both pH 2 and pH 4. This indicates that silica-associated functional groups play a role in the adsorption of Cr(VI) and Pb(II) through surface interactions and complexation [67]. Importantly, FT-IR analysis reveals significant weakening of the Mg–O stretching vibration, indicating its active participation in the formation of strongly bonded heavy metals (HM)–O groups [43]. At pH 2, (HM)–O groups were detected at specific wavenumbers: (799 and 499 $cm^{-1}$) in AR:MgO@$CBC_{Cr}$, 803 $cm^{-1}$ in AR:MgO@$CBC_{Pb}$, and (799 and 473 $cm^{-1}$) in AR:MgO@$CBC_{Cr-Pb}$ (Fig. 8(A)). Correspondingly, at pH 4, the wavenumbers were 475 $cm^{-1}$ (AR:MgO@$CBC_{Cr}$), 801 $cm^{-1}$ (AR:MgO@$CBC_{Pb}$), and 798 $cm^{-1}$ (AR:MgO@$CBC_{Cr-Pb}$) (Fig. 8(B)). Overall, the FTIR spectra confirm the involvement of O–H, C=O/C=C, and Si–O–Si functional groups, along with the emergence of new metal-oxygen (M–O) surface complexes and weakening of Mg–O bands. Thus, they highlight ligand exchange and complexation mechanisms via interactions between the adsorbate and the adsorbent.

Furthermore, XRD analysis displayed evidence of new diffraction peaks at pH 2 and 4 (Fig. 8(C) and (D)). For instance, at pH 2 in AR:MgO@$CBC_{Cr}$, new peaks were observed on 2θ at 43.37° and 62.86°, indicating crystalline structures of orthorhombic chromium silicide (CrSi)

and monoclinic magnesium chromate ($MgCrO_4$), corresponding to planes (210) and (220), with PDF# 51-1356 and 22-1148, respectively. The subsequent analysis at pH 4 revealed characteristic peaks analogous to those observed at pH 2, with the notable exception of the formation of hexagonal chromium disilicide ($CrSi_2$) at plane (111) on 2θ at 43.49°, consistent with PDF# 35-078. Moreover, AR:MgO@$CBC_{Pb}$ at pH 2 and 4 detected the formation of cubic $Mg_2Pb$ at plane (111) on 2θ at 45.27° with PDF# 23-0331, respectively. Notably, AR:MgO@$CBC_{Cr\text{-}Pb}$ at pH 2 exemplified a characteristic peak of orthorhombic lead chromate ($PbCrO_4$) on 2θ at 34.54° with PDF# 22-0385 at plane (020). Whereas two distinct peaks corresponding to $PbCrO_4$ emerged at pH 4, which were linked to the (211) plane (2θ angle: 26.66°, PDF# 38-1863) and the (020) plane, respectively. Moreover, a distinct peak of orthorhombic lead chlorate ($PbCl_2O_4$) was observed at plane (200) on 2θ at 43.64° with PDF# 25-0434.

In accordance, the formation of new compounds in XRD can be interpreted by chemical reactions. The findings suggest that a combination of surface complexation and reduction mechanisms may facilitate the formation of CrSi and $CrSi_2$. Initially, Cr(VI) species ($HCrO_4^-$) are reduced to Cr(III) under acidic conditions facilitated by the $Mg_2Si$-derived surface [68]. The resulting Cr(III) species are then adsorbed onto Si-rich active sites, where surface complexation occurs, leading to the formation of Cr-Si-associated (silicide-like) phases (Eqs. (7a-7c)). Meanwhile, the formation of $Mg_2Pb$ assisted by PbO may be ascribed to the ligand exchange mechanism, as illustrated in Eq. (8). Likewise, $MgCrO_4$ possibly formed through strong electrostatic attractions amongst $Mg^{2+}$ and $CrO_4^{2-}$ ions (Eq. 9) and $PbCrO_4$ formation likely resulted from electrostatic attraction as well as surface complexation (Eqs. (10, 11)). Previous study has also identified surface complexation as an operative process where Pb(II) ions interact with ionized oxygen-containing functional groups (–OH/–COO), resulting in Pb–O complex

formation (Eq. 10) [69]. Such formation of bimetallic complexes confirmed the synergistic removal of both Cr(VI) and Pb(II) in a binary solute system. In general, the findings from XRD analysis supported the dominant removal mechanisms identified in single solute system (Cr(VI): reduction, surface complexation and electrostatic attraction; Pb(II): ligand exchange/surface complexation and binary solute system (bimetallic bonding (Pb–O–Cr), electrostatic attraction, ligand exchange/surface complexation). The visual illustration of the proposed Cr(VI) and Pb(II) removal mechanism using MgO@CBC is presented in Fig. 9.

**Equations:**

$$Mg_2Si + 4H^+ \longrightarrow 2Mg^{2+} + Si - \text{rich surface} + 2H_2 \quad (7a)$$

$$HCrO_4^- + 7H^+ + 3e^- \longrightarrow Cr^{3+} + 4H_2O \quad (7b)$$

$$Cr^{3+} + Si - \text{surface} + 3e^- \longrightarrow Cr - Si\ (\text{surface} - \text{bound species}) \quad (7c)$$



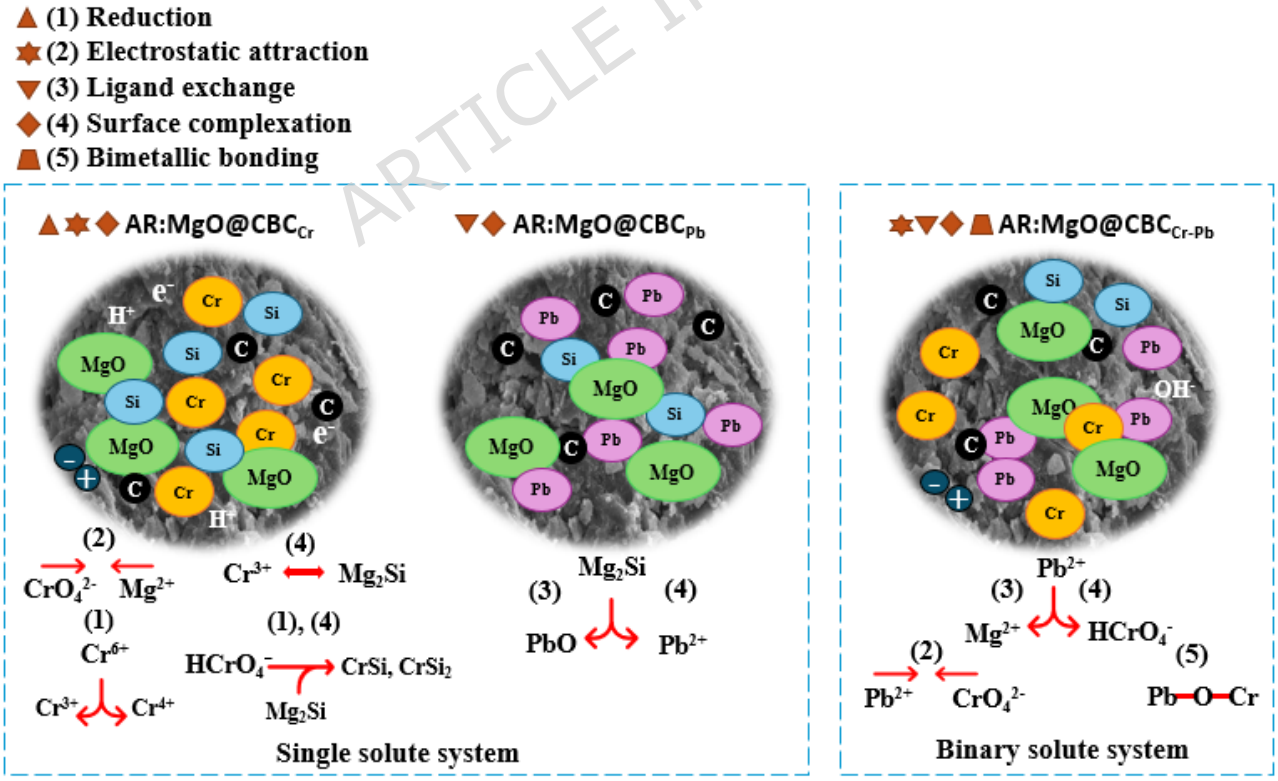


Fig. 9: Proposed mechanism of Cr(VI) and Pb(II) adsorption onto MgO@CBC.

$$2Mg_2Si + 4PbO \rightleftharpoons 2Mg_2Pb + 2Pb + 2SiO_2 \quad (8)$$

$$Mg^{2+} + CrO_4^{2-} \rightleftharpoons MgCrO_4 \quad (9)$$

$$Pb^{2+} + CrO_4^{2-} \rightleftharpoons PbCrO_4 \quad (10)$$

$$Pb^{2+} + HCrO_4^{2-} + OH^- \rightleftharpoons PbCrO_4 + H_2O \quad (11)$$

Hence, despite the comparatively low BET surface area of MgO@CBC (8.93 $m^2/g$, see Table 1), its impressive adsorption performance emphasizes the significant influence of surface chemical reactivity on metal ion uptake, as demonstrated by post-adsorption FTIR and XRD analyses.

## 3.5. Regeneration of MgO@CBC

The recyclability of MgO@CBC was evaluated through a series of adsorption-desorption experiments in a single-solute system (Cr(VI) at pH 2, Pb(II) at pH 4) and a binary-solute system (at pH 2 only), utilizing 100 mL of 1.0 M NaOH solution as the desorbing agent after every successive cycle. In the case of Cr(VI), strong alkaline conditions may have induced deprotonation of the MgO@CBC surface functional groups, generating abundant negative surface charges that could electrostatically repel the adsorbed anionic Cr(VI) species, thereby facilitating their release from the adsorbent surface. For Pb(II), alkaline treatment is considered to alter the surface charge characteristics of MgO@CBC, weakening the electrostatic and coordinative interactions between $Pb^{2+}$ ions and the adsorbent surface, consequently promoting desorption of the bound Pb(II)

species into solution [12]. Consequently, a gradual decline in removal efficiency and adsorption capacity across five cycles can be observed (Fig. 10). For Pb(II), removal efficiency decreased from 100% to 20.89% (single solute) and 99% to 0% (binary solute). Similarly, Cr(VI) removal decreased from 94% to 19.46% (single solute) and 88.5% to 6.1% (binary solute).



| Adsorbent | System | pH | Initial Conc. (mg/L) | Dosage (g/L) | Removal (%) | Adsorption capacity (mg/g) | Ref. |
|---|---|---|---|---|---|---|---|
| BPAC- $ZnCl_2$ + $Al_2O_3$ + Chitosan | Single<br>Ternary | 5.5 | 10 | 1 | Pb(II): 100<br>Pb(II): 85<br>Cu(II): 89<br>Cd(II): 27 | Pb(II): 39 | [70] |
| Banana peel-derived activated carbon | | | | | | | |
| CRHB-$ZnO_3$ | | | | | | I): 44.27 | [71] |
| ZnO-NPs modifie | | | | | | /I): 28.37 | |
| root husk biochar | | | | | | I): 42.05 | |
| | | | | | | II): 39.52 | |
| Mg-Fe LDH@OP | | | | | | 31.94 | [4] |
| Magnesium-iron l | | | | | | | |
| double hydroxide | | | | | | | |
| peel powder | | | | | | | |
| MgO-RHA | | | | | | 06.28 | [27] |
| MgO nanoparticle | | | | | | 68.72 | |
| husk ash | | | | | | | |
| MgO@BC | | | | | | 36.63 | [72] |
| MgO modified M | | | | | | | |
| organic fraction | | | | | | | |

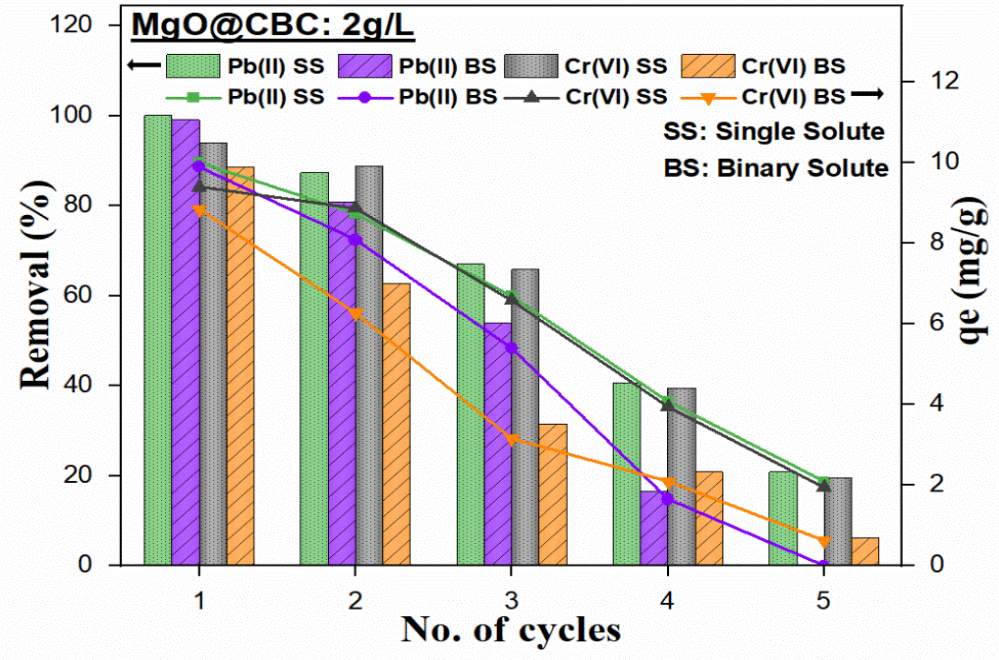


Fig. 10: Regeneration performance of MgO@CBC.

| Adsorbent | System | pH | Initial Conc. (mg/L) | Dosage (g/L) | Removal (%) | Adsorption capacity (mg/g) | Ref. |
|---|---|---|---|---|---|---|---|
| MgO@CBC | Single | 2 | 20 | 2 | Cr(VI): 94 | 22.02 | **This** |
| Banana peel + Rice husk | | 4 | | | Pb(II): 100 | 68.12 | **study** |
| (1:1) | Binary | 2 | | | Cr(VI): 88.5 | 31.74 | |
| | | | | | Pb(II): 99 | 29.88 | |

*NR = Not Reported*

In summary, MgO@CBC exhibits an antagonistic removal effect in regeneration in a binary solute system, thus underscoring the involvement of the following key factors: (1) progressive deactivation of active sites hindering Pb(II) and Cr(VI) binding upon regeneration, (2) ion exchange-mediated MgO content diminution during adsorption-desorption cycles, (3) surface property alterations caused by Pb(II) and Cr(VI) accumulation, (4) cumulative competitive inhibition between Cr(VI) and Pb(II) under limited active site availability, and (5) surface degradation and pore blockage due to repeated use [73]. Still, such a removal trend upon MgO@CBC regeneration up to five successive cycles indicates its suitability for the removal of coexisting contaminants from a heterogeneous wastewater environment.

**Table 3:** Comparison of adsorption performance of the present study with previously reported adsorbents.



## 3.5. Comparison with literature reported adsorbents

Table 3 compares the adsorption performance of MgO@CBC with previously reported adsorbents for the studied heavy metal ions. In single-component systems, MgO@CBC exhibited adsorption capacities of 22.02 mg/g for Cr(VI) and 68.12 mg/g for Pb(II). However, under binary conditions, these values changed to 31.74 mg/g for Cr(VI) and 29.88 mg/g for Pb(II), indicating a shift in uptake behavior due to competitive interactions between co-existing ions and changes in surface site availability. The marked decrease in Pb(II) adsorption capacity in the binary system suggests that Cr(VI)-related species preferentially interact with active sites, thereby limiting Pb(II) access to binding sites. Nevertheless, MgO@CBC maintains effective adsorption performance

under binary conditions, suggesting its potential for further investigation in more complex aqueous environments.

## 4. Conclusions

In current research, we explored the Cr(VI) and Pb(II) adsorption efficacy of various raw and MgO activated (co)pyrolyzed biochar materials derived from rice husk and banana peels. In comparison to other synthesized biochar, MgO@CBC outperformed in eliminating Cr(VI) and Pb(II) from synthetic solutions due to the unique combination of its structural and surface characteristics and was therefore comprehensively investigated. The primary findings are outlined as follows:

- In a single solute system, Cr(VI) removal up to 96% at pH 2 and complete Pb(II) removal at pH 4 was observed under boundary conditions of 2 g/L dosage, 20 mg/L metal ion concentration, and 120-minute contact time.
- The binary system demonstrated a removal efficiency of 88.5% for Cr(VI) and 99% for Pb(II) at pH 2, using experimental parameters like those employed in the single solute system. Similarly, synergistic adsorption performance of Cr(VI) at pH 4 and Pb(II) at pH 2 were also observed in binary solute system upon increasing contaminant loading.
- The Freundlich isotherm primarily described the adsorption behavior in the binary system, suggesting heterogeneous multilayer adsorption. However, an exception was noted for Cr(VI) at pH 2 and a dosage of 4 g/L, where the adsorption conformed to the Langmuir model.
- MgO@CBC presented dominant removal pathways in single solute system as (Cr(VI): reduction coupled with electrostatic attraction) and (Pb(II): ligand exchange followed by surface complexation) and in binary system as (Cr(VI) and Pb(II): ligand exchange,

electrostatic attraction, bimetallic bonding (Pb-O-Cr) and surface complexation) leading to enhance bimetallic adsorption performance from surrogated wastewater.

- Overall, the adsorption performance was primarily controlled by surface chemistry and the availability of active functional sites on the adsorbent surface.
- The regeneration results indicate that MgO@CBC retains its adsorption capability over multiple cycles, highlighting its potential for practical application.

In general, these results revealed excellent adsorption capability of our synthesized novel MgO@CBC for Cr(VI) and Pb(II) under a bimetallic environment, which is a clear indication of its potential performance in complex real wastewater systems. Thus, it may offer a sustainable, environmentally friendly solution to industries, particularly tanneries, when dealing with toxic contaminants from their effluents.



## Appendix A. Supplementary data

Supplementary data associated with this article can be found in the online version.

## Funding

This research did not receive any external funding.

## Acknowledgement

This study was supported by the Research Fund of the National University of Sciences and Technology (NUST), Pakistan, and The Catholic University of Korea, Republic of Korea. The authors also gratefully acknowledge Ms. Shahida Riaz, Lecturer in English, HITEC University, Pakistan, for carefully reviewing the manuscript for language and grammatical accuracy.

## Declaration of Competing Interest

The authors have nothing to declare.

**Data Availability**

All data generated or analyzed during this study are included in this published article and its supplementary information files.

## References

[1] T. A. Saleh, M. Mustaqeem, and M. Khaled, "Water treatment technologies in removing heavy metal ions from wastewater: A review," May 01, 2022, *Elsevier B.V.* doi: 10.1016/j.enmm.2021.100617.

[2] M. Afzal, G. Shabir, S. Iqbal, T. Mustafa, Q. M. Khan, and Z. M. Khalid, "Assessment of Heavy Metal Contamination in Soil and Groundwater at Leather Industrial Area of Kasur, Pakistan," *Clean (Weinh).*, vol. 42, no. 8, pp. 1133–1139, 2014, doi: 10.1002/clen.201100715.

[3] T. A. Chandio, M. N. Khan, M. T. Muhammad, O. Yalcinkaya, E. Turan, and A. F. Kayis, "Health risk assessment of chromium contamination in the nearby population of mining plants, situated at Balochistan, Pakistan", doi: 10.1007/s11356-020-11649-4/Published.

[4] W. Usmani *et al.*, "Efficient removal of hexavalent chromium Cr (VI) using magnesium-iron layered double hydroxide supported on orange peel (Mg-Fe LDH@OPP): A synthetic experimental and mechanism studies," *Journal of Water Process Engineering*, vol. 55, Oct. 2023, doi: 10.1016/j.jwpe.2023.104233.

[5] V. Kumar, S. K. Dwivedi, and S. Oh, "A critical review on lead removal from industrial wastewater: Recent advances and future outlook," Feb. 01, 2022, *Elsevier Ltd*. doi: 10.1016/j.jwpe.2021.102518.

[6] P. Sharma, S. P. Singh, S. K. Parakh, and Y. W. Tong, "Health hazards of hexavalent chromium (Cr (VI)) and its microbial reduction," 2022, *Taylor and Francis Ltd.* doi: 10.1080/21655979.2022.2037273.

[7] R. Shrestha *et al.*, "Technological trends in heavy metals removal from industrial wastewater: A review," Aug. 01, 2021, *Elsevier Ltd*. doi: 10.1016/j.jece.2021.105688.

[8] I. R. Chowdhury, S. Chowdhury, M. A. J. Mazumder, and A. Al-Ahmed, "Removal of lead ions (Pb2+) from water and wastewater: a review on the low-cost adsorbents," Aug. 01, 2022, *Springer Science and Business Media Deutschland GmbH*. doi: 10.1007/s13201-022-01703-6.

[9] A. Ali, S. Alharthi, N. H. Al-Shaalan, A. Naz, and H. J. S. Fan, "Efficient Removal of Hexavalent Chromium (Cr(VI)) from Wastewater Using Amide-Modified Biochar," *Molecules*, vol. 28, no. 13, Jul. 2023, doi: 10.3390/molecules28135146.

[10] D. Mahlangu, K. Mphahlele, F. De Paola, and N. H. Mthombeni, "Microalgae-Mediated Biosorption for Effective Heavy Metals Removal from Wastewater: A Review," Mar. 01, 2024, *Multidisciplinary Digital Publishing Institute (MDPI)*. doi: 10.3390/w16050718.

[11] E. B. Hussein, F. A. Rasheed, A. S. Mohammed, and K. F. Kayani, "Emerging nanotechnology approaches for sustainable water treatment and heavy metals removal: a comprehensive review," *RSC Adv.*, vol. 15, no. 48, pp. 41061–41107, 2025, doi: 10.1039/d5ra06914a.

[12] N. Wang *et al.*, "Engineered biochar for simultaneous removal of heavy metals and organic pollutants from wastewater: mechanisms, efficiency, and applications," *Biochar X*, vol. 1, no. 1, pp. 0–0, 2025, doi: 10.48130/bchax-0025-0008.

[13] P. Liu, L. Boffa, and G. Cravotto, "Biochar Derived from Agricultural Residues for Wastewater Contaminant Removal," Jan. 01, 2026, *Multidisciplinary Digital Publishing Institute (MDPI)*. doi: 10.3390/su18010435.

[14] H. Znad, M. R. Awual, and S. Martini, "The Utilization of Algae and Seaweed Biomass for Bioremediation of Heavy Metal-Contaminated Wastewater," Feb. 01, 2022, *MDPI*. doi: 10.3390/molecules27041275.

[15] K. Dogo *et al.*, "Effect of mixing ratio on magnetite-incorporated MWCNTs for enhanced heavy metal ions adsorption from petroleum-contaminated wastewater," *Microporous and Mesoporous Materials*, vol. 404, Mar. 2026, doi: 10.1016/j.micromeso.2026.114034.

[16] R. K. T. M. Y. Binu Kumari, "Effect of poly-aniline coated iron ore mining waste (PANI@IOMW) as efficient adsorbent on mitigation of Cr (VI) from aqueous solution: Experimental and statistical investigation," *Chemical Engineering Research and Design*, vol. 190, pp. 434–450, 2023.

[17] Z. Hashmi, A. S. Jatoi, S. Nadeem, A. Anjum, S. M. Imam, and H. Jangda, "Comparative analysis of conventional to biomass-derived adsorbent for wastewater treatment: a review," Jan. 01, 2024, *Springer Science and Business Media Deutschland GmbH*. doi: 10.1007/s13399-022-02443-y.

[18] A. Ashfaq *et al.*, "Efficient adsorption of lead ions from synthetic wastewater using agrowaste-based mixed biomass (Potato peels and banana peels)," *Water (Switzerland)*, vol. 13, no. 23, Dec. 2021, doi: 10.3390/w13233344.

[19] A. Ali, S. Alharthi, N. H. Al-Shaalan, A. Naz, and H. J. S. Fan, "Efficient Removal of Hexavalent Chromium (Cr(VI)) from Wastewater Using Amide-Modified Biochar," *Molecules*, vol. 28, no. 13, Jul. 2023, doi: 10.3390/molecules28135146.

[20] R. M. A. K. A. K. M. A. & S. K. Z. Raji, “Biosorption of lead from water using fruit and vegetable peels: characteristics, adsorption kinetics, and isotherms,” *International journal of environmental science and technology*, vol. 22, pp. 15775–15790, Aug. 2025.

[21] S. Chakma, M. Hasan, S. K. Rakshit, J. Kozinski, and K. Kang, “Review of recent advances in the design, synthesis, and modification of biochar for remediation of heavy metal pollution in water,” Apr. 01, 2025, *John Wiley and Sons Inc*. doi: 10.1002/cjce.25693.

[22] T. M. Tichem, Y. Wang, R. B. H. Gameli, B. Mbage, and B. Li, “Multicomponent Adsorption of Pollutants from Wastewater Using Low-Cost Eco-Friendly Iron-Modified Rice Husk Biochar in the Era of Green Chemistry,” *Sustainability (Switzerland)*, vol. 15, no. 23, Dec. 2023, doi: 10.3390/su152316348.

[23] N. A. Negm, A. A. Altalhi, H. M. Ahmed, and E. A. Mohamed, “Synergistic effect of rice husk-derived activated carbon modified by Ni/Al-layered double hydroxides for lead removal from industrial wastewater,” *Sci. Rep.*, vol. 14, no. 1, Dec. 2024, doi: 10.1038/s41598-024-77569-2.

[24] H. A. Areti, A. Jabesa, B. J. Daba, and D. Jibril, “Response surface method based parametric optimization of Cr(VI) removal from tannery wastewater using a mixed banana peel and corn cob activated carbon: Kinetic and isotherm modeling studies,” *Journal of Water Process Engineering*, vol. 59, Mar. 2024, doi: 10.1016/j.jwpe.2024.104977.

[25] Y. tao Sun, J. dong Chen, Z. hua Wei, Y. kai Chen, C. lei Shao, and J. feng Zhou, “Copper ion removal from aqueous media using banana peel biochar/Fe3O4/branched polyethyleneimine,” *Colloids Surf. A Physicochem. Eng. Asp.*, vol. 658, Feb. 2023, doi: 10.1016/j.colsurfa.2022.130736.

[26] M. Jain, M. Yadav, T. Kohout, M. Lahtinen, V. K. Garg, and M. Sillanpää, "Development of iron oxide/activated carbon nanoparticle composite for the removal of Cr(VI), Cu(II) and Cd(II) ions from aqueous solution," *Water Resour. Ind.*, vol. 20, pp. 54–74, Dec. 2018, doi: 10.1016/j.wri.2018.10.001.

[27] L. S. Mustapha, S. O. Jacob-Oricha, M. D. Yahya, S. Y. Lau, A. S. Yusuff, and K. S. Obayomi, "Effective removal of Cr(VI) and Pb(II) ions from mining wastewater using eco-friendly synthesized magnesium oxide nanoparticles incorporated rice husk ash," *Environmental Advances*, vol. 15, Apr. 2024, doi: 10.1016/j.envadv.2024.100507.

[28] A. Li, Y. Zhang, W. Ge, Y. Zhang, L. Liu, and G. Qiu, "Removal of heavy metals from wastewaters with biochar pyrolyzed from MgAl-layered double hydroxide-coated rice husk: Mechanism and application," *Bioresour. Technol.*, vol. 347, Mar. 2022, doi: 10.1016/j.biortech.2021.126425.

[29] A. Li *et al.*, "Resource utilization of rice husk biomass: Preparation of MgO flake-modified biochar for simultaneous removal of heavy metals from aqueous solution and polluted soil," *Environmental Pollution*, vol. 310, Oct. 2022, doi: 10.1016/j.envpol.2022.119869.

[30] M. Rabiee Abyaneh, G. Nabi Bidhendi, and A. Daryabeigi Zand, "Pb(II), Cd(II), and Mn(II) adsorption onto pruning-derived biochar: physicochemical characterization, modeling and application in real landfill leachate," *Sci. Rep.*, vol. 14, no. 1, Dec. 2024, doi: 10.1038/s41598-024-54028-6.

[31] A. Li, Y. Zhang, W. Ge, Y. Zhang, L. Liu, and G. Qiu, "Removal of heavy metals from wastewaters with biochar pyrolyzed from MgAl-layered double hydroxide-coated rice husk: Mechanism and application," *Bioresour. Technol.*, vol. 347, Mar. 2022, doi: 10.1016/j.biortech.2021.126425.

[32] S. Cheng *et al.*, "High-efficiency removal of lead/cadmium from wastewater by MgO modified biochar derived from crofton weed," *Bioresour. Technol.*, vol. 343, Jan. 2022, doi: 10.1016/j.biortech.2021.126081.

[33] P. Hao *et al.*, "MgO-embedded S-doped porous biochar composites for efficient removal Cd(II) and Pb(II) in water: DFT studies and mechanistic insights," *Sep. Purif. Technol.*, vol. 363, Aug. 2025, doi: 10.1016/j.seppur.2025.132079.

[34] Y. Du, S. Wu, T. Feng, and W. Jiang, "MgO-Loaded Magnetic Crab Shell-Derived Biochar for Efficient Synergistic Adsorption of Heavy Metals and Dye: Characterization, Adsorption Performance and Mechanistic Study," *Nanomaterials*, vol. 16, no. 3, Feb. 2026, doi: 10.3390/nano16030214.

[35] N. Hossain, S. Nizamuddin, G. Griffin, P. Selvakannan, N. M. Mubarak, and T. M. I. Mahlia, "Synthesis and characterization of rice husk biochar via hydrothermal carbonization for wastewater treatment and biofuel production," *Sci. Rep.*, vol. 10, no. 1, Dec. 2020, doi: 10.1038/s41598-020-75936-3.

[36] M. Shafiq, A. A. Alazba, and M. T. Amin, "Preparation of ZnMgAl-Layered Double Hydroxide and Rice Husk Biochar Composites for Cu(II) and Pb(II) Ions Removal from Synthetic Wastewater," *Water (Switzerland)*, vol. 15, no. 12, Jun. 2023, doi: 10.3390/w15122207.

[37] T. N. T. Izhar *et al.*, "Adsorption of hydrogen sulfide (H2s) from municipal solid waste by using biochars," *Biointerface Res. Appl. Chem.*, vol. 12, no. 6, pp. 8057–8069, Dec. 2022, doi: 10.33263/BRIAC126.80578069.

[38] A. K. Priya *et al.*, "Investigation of mechanism of heavy metals (Cr6+, Pb2+& Zn2+) adsorption from aqueous medium using rice husk ash: Kinetic and thermodynamic approach," *Chemosphere*, vol. 286, Jan. 2022, doi: 10.1016/j.chemosphere.2021.131796.

[39] R. Foroutan, S. J. Peighambardoust, R. Mohammadi, S. H. Peighambardoust, and B. Ramavandi, "Cadmium ion removal from aqueous media using banana peel biochar/Fe3O4/ZIF-67," *Environ. Res.*, vol. 211, Aug. 2022, doi: 10.1016/j.envres.2022.113020.

[40] H. Deng, S. Zhang, Q. Li, A. Li, W. Gan, and L. Hu, "Efficient Removal of Lead, Cadmium, and Zinc from Water and Soil by MgFe Layered Double Hydroxide: Adsorption Properties and Mechanisms," *Sustainability*, vol. 16, no. 24, p. 11037, Dec. 2024, doi: 10.3390/su162411037.

[41] X. Qin, J. Luo, Z. Liu, and Y. Fu, "Preparation and characterization of mgo-modified rice straw biochars," *Molecules*, vol. 25, no. 23, Dec. 2020, doi: 10.3390/molecules25235730.

[42] H. Adugna Areti, A. Jabesa, M. Diriba Muleta, and A. Nemera Emana, "Adsorptive performances and valorization of green synthesized biochar–based activated carbon from banana peel and corn cob composites for the abatement of Cr(VI) from synthetic solutions: Parameters, isotherms, and remediation studies," *Heliyon*, vol. 10, no. 13, Jul. 2024, doi: 10.1016/j.heliyon.2024.e33811.

[43] A. Li *et al.*, "Resource utilization of rice husk biomass: Preparation of MgO flake-modified biochar for simultaneous removal of heavy metals from aqueous solution and polluted soil," *Environmental Pollution*, vol. 310, Oct. 2022, doi: 10.1016/j.envpol.2022.119869.

[44] R. Amen *et al.*, "Lead and cadmium removal from wastewater using eco-friendly biochar adsorbent derived from rice husk, wheat straw, and corncob," *Clean. Eng. Technol.*, vol. 1, Dec. 2020, doi: 10.1016/j.clet.2020.100006.

[45] J. Lugo-Arias, J. González-Álvarez, and A. Maturana, "Mg-impregnated rice husk biochar in fixed-bed columns: high-capacity continuous-flow removal of nitrate and phosphate from wastewater," *Biomass Convers. Biorefin.*, vol. 16, no. 4, Feb. 2026, doi: 10.1007/s13399-026-07093-y.

[46] W. Chen *et al.*, "A green and economical MgO/biochar composite for the removal of U(VI) from aqueous solutions," *Chemical Engineering Research and Design*, vol. 180, pp. 391–401, Apr. 2022, doi: 10.1016/j.cherd.2022.02.031.

[47] E. Scapin *et al.*, "Activated carbon from rice husk biochar with high surface area," *Biointerface Res. Appl. Chem.*, vol. 11, no. 3, pp. 10265–10277, 2021, doi: 10.33263/BRIAC113.1026510277.

[48] E. Khoshnood Motlagh, S. Sharifian, and N. Asasian-Kolur, "Alkaline activating agents for activation of rice husk biochar and simultaneous bio-silica extraction," *Bioresour. Technol. Rep.*, vol. 16, Dec. 2021, doi: 10.1016/j.biteb.2021.100853.

[49] Y. Xu, H. Xia, Q. Zhang, G. Jiang, W. Cai, and W. Hu, "Adsorption of cadmium(II) in wastewater by magnesium oxide modified biochar," *Arabian Journal of Chemistry*, vol. 15, no. 9, Sep. 2022, doi: 10.1016/j.arabjc.2022.104059.

[50] J. Xiang *et al.*, "Enhanced adsorption of Cd(II) from aqueous solution by a magnesium oxide–rice husk biochar composite," *Environmental Science and Pollution Research*, vol. 25, no. 14, pp. 14032–14042, May 2018, doi: 10.1007/s11356-018-1594-1.

[51] D. T. Tran *et al.*, "A facile technique to prepare MgO-biochar nanocomposites for cationic and anionic nutrient removal," *Journal of Water Process Engineering*, vol. 47, Jun. 2022, doi: 10.1016/j.jwpe.2022.102702.

[52] J. Xiao *et al.*, "Synthesis of MgO-Coated Canna Biochar and Its Application in the Treatment of Wastewater Containing Phosphorus," *Water (Switzerland)*, vol. 16, no. 6, Mar. 2024, doi: 10.3390/w16060873.

[53] G. Murtaza *et al.*, "Recent trends and economic significance of modified/functionalized biochars for remediation of environmental pollutants," *Sci. Rep.*, vol. 14, no. 1, Dec. 2024, doi: 10.1038/s41598-023-50623-1.

[54] P. E. Hock, A. N. M. Faizal, L. Sirajo, and M. A. A. Zaini, "Insight into kinetics, equilibrium, and thermodynamics of malachite green adsorption onto banana peel adsorbents," *Biomass Convers. Biorefin.*, vol. 14, no. 15, pp. 17405–17421, Aug. 2024, doi: 10.1007/s13399-023-04117-9.

[55] X. Zhao, J. Hu, Y. Yang, M. Liu, and H. Wang, "Enhanced Cr(VI) removal from water by Fe-modified sewage sludge biochar: Influencing factors and mechanisms," *J. Environ. Chem. Eng.*, vol. 13, no. 5, Oct. 2025, doi: 10.1016/j.jece.2025.117501.

[56] M. Jain, V. K. Garg, and K. Kadirvelu, "Adsorption of hexavalent chromium from aqueous medium onto carbonaceous adsorbents prepared from waste biomass," *J. Environ. Manage.*, vol. 91, no. 4, pp. 949–957, 2010, doi: 10.1016/j.jenvman.2009.12.002.

[57] M. Erdem and A. Öner, "Preparation and Characterization of Low-Cost Bio-Sorbent and a Novel Activated Carbon from Agro-Wastes for Efficient Cr(VI) Removal," *Water Air Soil Pollut.*, vol. 236, no. 5, May 2025, doi: 10.1007/s11270-025-07910-6.

[58] E. C. Emenike *et al.*, "Adsorptive removal of Cr(VI) and Pb(II) using biochar from biomass and plastic waste: characterization and performance evaluation," *Biomass Bioenergy*, vol. 207, Apr. 2026, doi: 10.1016/j.biombioe.2025.108722.

[59] S. Cheng *et al.*, "High-efficiency removal of lead/cadmium from wastewater by MgO modified biochar derived from crofton weed," *Bioresour. Technol.*, vol. 343, Jan. 2022, doi: 10.1016/j.biortech.2021.126081.

[60] A. Li, H. Deng, Y. Jiang, and C. Ye, "High-efficiency removal of Cr (VI) from wastewater by Mg-loaded biochars: Adsorption process and removal mechanism," *Materials*, vol. 13, no. 4, Feb. 2020, doi: 10.3390/ma13040947.

[61] M. M. Hammo, T. Akar, F. Sayin, S. Celik, and S. T. Akar, "Efficacy of green waste-derived biochar for lead removal from aqueous systems: Characterization, equilibrium, kinetic and application," *J. Environ. Manage.*, vol. 289, Jul. 2021, doi: 10.1016/j.jenvman.2021.112490.

[62] L. Liu *et al.*, "Adsorption characteristics and mechanism of Pb(II) by agricultural waste-derived biochars produced from a pilot-scale pyrolysis system," *Waste Management*, vol. 100, pp. 287–295, Dec. 2019, doi: 10.1016/j.wasman.2019.08.021.

[63] L. Sellaoui, H. Wang, M. Badawi, A. Bonilla-Petriciolet, and Z. Chen, "Synergistic adsorption of Pb2+ and CrO42− on an engineered biochar highlighted by statistical physical modeling," *J. Mol. Liq.*, vol. 312, Aug. 2020, doi: 10.1016/j.molliq.2020.113483.

[64] M. Jain, V. K. Garg, K. Kadirvelu, and M. Sillanpää, "Adsorption of heavy metals from multi-metal aqueous solution by sunflower plant biomass-based carbons," *International Journal of Environmental Science and Technology*, vol. 13, no. 2, pp. 493–500, Feb. 2016, doi: 10.1007/s13762-015-0855-5.

[65] Y. Venkatraman *et al.*, "Exploring Modified Rice Straw Biochar as a Sustainable Solution for Simultaneous Cr(VI) and Pb(II) Removal from Wastewater: Characterization, Mechanism Insights, and Application Feasibility," *ACS Omega*, vol. 8, no. 41, pp. 38130–38147, Oct. 2023, doi: 10.1021/acsomega.3c04271.

[66] Q. Shi *et al.*, "Efficient performance of magnesium oxide loaded biochar for the significant removal of Pb2+ and Cd2+ from aqueous solution," *Ecotoxicol. Environ. Saf.*, vol. 221, Sep. 2021, doi: 10.1016/j.ecoenv.2021.112426.

[67] A. K. I. Flores-Trujillo, A. G. Morales-Mendoza, and R. Rodríguez-Vázquez, "Behavior of a Mixture of Metals for Competiting Adsorption Sites of Untreated and Alkali-Treated Rice Husk," *Processes*, vol. 12, no. 7, Jul. 2024, doi: 10.3390/pr12071299.

[68] H. Adugna Areti, A. Jabesa, M. Diriba Muleta, and A. Nemera Emana, "Adsorptive performances and valorization of green synthesized biochar–based activated carbon from banana peel and corn cob composites for the abatement of Cr(VI) from synthetic solutions: Parameters, isotherms, and remediation studies," *Heliyon*, vol. 10, no. 13, Jul. 2024, doi: 10.1016/j.heliyon.2024.e33811.

[69] S. F. Tang *et al.*, "Adsorption Characteristics and Mechanisms of Fe-Mn Oxide Modified Biochar for Pb(II) in Wastewater," *Int. J. Environ. Res. Public Health*, vol. 19, no. 14, Jul. 2022, doi: 10.3390/ijerph19148420.

[70] V. Thi Thanh Tran, O. Nakagoe, H. Sano, S. Tanabe, and K. Kamada, "Optimized composition of banana peel-derived activated carbon modified with aluminum oxide and chitosan for enhanced adsorption of Pb(II), Cu(II), and Cd(II) in wastewater treatment," *Appl. Water Sci.*, vol. 15, no. 9, Sep. 2025, doi: 10.1007/s13201-025-02592-1.

[71] P. T. Tho *et al.*, "Enhanced simultaneous adsorption of As(iii), Cd(ii), Pb(ii) and Cr(vi) ions from aqueous solution using cassava root husk-derived biochar loaded with ZnO nanoparticles," *RSC Adv.*, vol. 11, no. 31, pp. 18881–18897, May 2021, doi: 10.1039/d1ra01599k.

[72] N. S. Dlamini, P. K. Jha, and P. K. Sharma, "Magnesium oxide-functionalized biochar synthesis from municipal solid waste for Pb(II) removal in aqueous media and potential application in leachate remediation," *Environmental Science and Pollution Research*, Feb. 2026, doi: 10.1007/s11356-026-37461-0.

[73] Y. Xu, H. Xia, Q. Zhang, G. Jiang, W. Cai, and W. Hu, "Adsorption of cadmium(II) in wastewater by magnesium oxide modified biochar," *Arabian Journal of Chemistry*, vol. 15, no. 9, Sep. 2022, doi: 10.1016/j.arabjc.2022.104059.

**Author Contributions Statement**

**Tayyaba Kanwal:** Conceptualization, Data curation, Investigation, Methodology, Software, Writing – original draft. **Rashid Iftikhar:** Formal analysis, Validation, Writing – review & editing. **Mathias Ernst:** Formal analysis, Visualization, Writing – review & editing. **Kang Hoon Lee:** Formal analysis, Resources, Writing – review & editing. **Muhammad Ali Inam:** Conceptualization, Methodology, Project administration, Resources, Supervision, Writing – review & editing.